



HAL
open science

Cellular Heterogeneity in Pressure and Growth Emerges from Tissue Topology and Geometry

Yuchen Long, Ibrahim Cheddadi, Gabriella Mosca, Vincent Mirabet, Mathilde Dumond, Annamaria Kiss, Jan Traas, Christophe Godin, Arezki Boudaoud

► **To cite this version:**

Yuchen Long, Ibrahim Cheddadi, Gabriella Mosca, Vincent Mirabet, Mathilde Dumond, et al.. Cellular Heterogeneity in Pressure and Growth Emerges from Tissue Topology and Geometry. *Current Biology - CB*, 2020, 30 (8), pp.1504-1516.e8. 10.1016/j.cub.2020.02.027. hal-03029965

HAL Id: hal-03029965

<https://hal.science/hal-03029965>

Submitted on 22 Aug 2022

HAL is a multi-disciplinary open access archive for the deposit and dissemination of scientific research documents, whether they are published or not. The documents may come from teaching and research institutions in France or abroad, or from public or private research centers.

L'archive ouverte pluridisciplinaire **HAL**, est destinée au dépôt et à la diffusion de documents scientifiques de niveau recherche, publiés ou non, émanant des établissements d'enseignement et de recherche français ou étrangers, des laboratoires publics ou privés.



Distributed under a Creative Commons Attribution - NonCommercial - NoDerivatives 4.0 International License

1 **Title:**

2 **Cellular heterogeneity in pressure and growth emerges from tissue**
3 **topology and geometry**

4 Yuchen Long^{1,*}, Ibrahim Cheddadi², Gabriella Mosca³, Vincent Mirabet^{1,4}, Mathilde
5 Dumond^{1,5}, Annamaria Kiss¹, Jan Traas¹, Christophe Godin¹, Arezki Boudaoud^{1,6*}.

6 1. Laboratoire Reproduction et Développement des Plantes, Université de Lyon, ENS de
7 Lyon, UCB Lyon 1, CNRS, INRAe, INRIA, F-69342, Lyon, France.

8 2. Univ. Grenoble Alpes, CNRS, Grenoble INP, TIMC-IMAG, 38000 Grenoble, France.

9 3. Department of Plant and Microbial Biology, University of Zürich, Zollikerstrasse 107,
10 CH-8008 Zürich, Switzerland.

11 4. Lycée A. et L. Lumière, F-69372 Lyon Cedex 08, France.

12 5. Current address: MD Systems GmbH, CH-8048 Zürich

13 6. Lead contact.

14 *. Correspondence to yuchen.long@ens-lyon.fr or arezki.boudaoud@ens-lyon.fr

15 The authors declare no competing financial interests.

16

17

18 **Key words**

19 Cellular heterogeneity, hydrostatic pressure, tissue topology, growth mechanics, tissue
20 hydraulics, atomic force microscopy, biophysical modelling.

21 **Summary**

22 Cell-to-cell heterogeneity prevails in many systems, as exemplified by cell growth, although
23 the origin and function of such heterogeneity are often unclear. In plants, growth is physically
24 controlled by cell wall mechanics and cell hydrostatic pressure, alias turgor pressure. Whereas
25 cell wall heterogeneity has received extensive attention, the spatial variation of turgor
26 pressure is often overlooked. Here, combining atomic force microscopy and a physical model
27 of pressurized cells, we show that turgor pressure is heterogeneous in the Arabidopsis shoot
28 apical meristem, a population of stem cells that generates all plant aerial organs. In contrast
29 with cell wall mechanical properties that appear to vary stochastically between neighbouring
30 cells, turgor pressure anticorrelates with cell size and cell neighbour number (local topology),
31 in agreement with the prediction by our model of tissue expansion, which couples cell wall
32 mechanics and tissue hydraulics. Additionally, our model predicts two types of correlations
33 between pressure and cellular growth rate, where high pressure may lead to faster- or slower-
34 than-average growth, depending on cell wall extensibility, yield threshold, osmotic pressure,
35 and hydraulic conductivity. The meristem exhibits one of these two regimes depending on
36 conditions, suggesting that, in this tissue, water conductivity may contribute to growth
37 control. Our results unravel cell pressure as a source of patterned heterogeneity and illustrate
38 links between local topology, cell mechanical state and cell growth, with potential roles in
39 tissue homeostasis.

40

41 **Introduction**

42 Cell-to-cell fluctuations are observed in many biological processes like gene expression,
43 signalling, cell size regulation and growth [1–8]. Notably, heterogeneity in cell size and
44 growth rate often prevails and may impact tissue patterning and macroscopic growth
45 robustness [1,2]. Cell volume change is driven by osmosis [9–11] and the resulting
46 intracellular hydrostatic pressure, and is restrained by peripheral constraints — plasma
47 membrane, cytoskeletal cortex, extracellular matrix, or cell wall — in plant cells [12], animal
48 cells [13] including tumorous [14], and microbial cells [15] (Figure 1A).

49 Due to high difference between internal and external osmotic potential, cells with rigid cell
50 walls – like in plants, bacteria and fungi – accumulate hydrostatic pressure, alias turgor
51 pressure, often greater than atmospheric pressure (Figure S1A and S1B) [12]. Animal cells
52 also accumulate hydrostatic pressure, especially when compacted or contracting [13,14],
53 though to a lesser extent than walled cells. Whereas it is increasingly realized that pressure
54 regulation is crucial for general physiology, growth and signalling in animal [9,11,13] and
55 plant cells [16–19], pressure remains poorly characterized in multicellular contexts.

56 In plants, turgor pressure drives cell expansion, which is classically modelled as visco-elasto-
57 plastic process, as depicted in the Lockhart-Ortega equation (Figure 1B) [20]: The cell
58 expands irreversibly whenever turgor pressure, P , is higher than a threshold “yield pressure”,
59 P^Y , and growth rate is proportional to extensibility (a measure of how easily the wall expands
60 irreversibly) and to $P - P^Y$. When $P < P^Y$, the cell behaves elastically, returning to its initial
61 volume after a transient change in pressure (Figure 1B). However, other experimental
62 observations in single-cell systems suggest that growth rate and pressure level are not always
63 associated — growth rate of *E. coli* is insensitive to variations in turgor pressure [15] and
64 growth rate oscillations in pollen tube likely occur at constant pressure [21] — making it
65 difficult to understand the link between growth regulation and cellular pressure.

66 In multicellular context, like the plant shoot apex and sepal epidermis, neighbouring cells
67 grow at notably different rates [1]. This prompts the question, according to the Lockhart-
68 Ortega equation, whether turgor pressure also varies between neighbouring plant cells.

69 Intuitively, pressure difference should be equalized by plasmodesmata, symplasmic bridges
70 connecting most plant cells [22]. This is supported by correlated plasmodesmata closing
71 (symplasmic isolation) and pressure build-up in specialized cells, like guard cells and cotton
72 fibres [23–25]. However, pressure gradient was also observed in plant tissues with
73 symplasmic continuity [26], and predicted to be crucial for perception by roots of water
74 availability [27]. Additionally, computational models of tissue mechanics suggest that
75 neighbouring cells need to have different pressure to recapitulate tissue arrangement and
76 mechanical status in chemical-treated *Arabidopsis* epidermis [28] and in *Drosophila* epithelia
77 [29], although such spatial variation is yet to be demonstrated, and its relation with cell-to-cell
78 growth variability remains elusive.

79 Here, we explore this issue in a model plant tissue, the epidermis of the *Arabidopsis thaliana*
80 shoot apical meristem (SAM), by combining computational modelling, dimensional analysis,
81 and experimental observations. Based on our results, we propose a link between cell topology,
82 cell size, and cell hydro-mechanical status that may be involved in tissue homeostasis.

83 **Results**

84 **A mechanical-hydraulic model predicts pressure heterogeneity emerging from tissue** 85 **arrangement**

86 Earlier tissue models [28,29] retrieved intracellular pressure from static tissue geometry or
87 required differences in osmotic pressure between cells, whereas a recent model by Cheddadi
88 et al. proposed that both hydrostatic pressure and growth emerge from the coupling between
89 cell wall mechanics and classic plant hydraulics [30] in a tissue with hexagonal topology, i.e.
90 with every cell having six neighbours. We therefore tested, based on this model (Figure 1C-
91 1F), the consequences of unequal neighbour numbers on the mechanical status of the tissue,
92 and notably on pressure. The model generalizes the Lockhart-Ortega equation of visco-elasto-
93 plastic 1D growth of single cell (Figure 1B) [20], by assuming that each cell wall has a
94 thickness w and behaves as an elastic material when wall strain (elastic deformation), ε ,
95 induced by turgor pressure is lower than a threshold ε^Y . When wall tension is large enough
96 (when wall strain exceeds ε^Y), the cell wall undergoes irreversible expansion, akin to visco-

97 plastic flow, with an extensibility Φ^w (Figure 1F). The higher Φ^w , the faster the wall expands
98 for a given tension. Water flux from extracellular space is proportional to the conductivity of
99 the cell membrane per unit surface, L^a , and to the cross-membrane water potential (chemical
100 potential of water) difference, $\Delta\Pi - P$, which involves the cross-membrane difference in
101 osmotic pressure, $\Delta\Pi$ (Figure 1D). For parsimony, we assume no differences in osmotic
102 pressure between cells, so that $\Delta\Pi$ is set constant. Intercellular water redistribution via plant
103 plasmodesmata [31], animal gap junctions, or cytoplasmic bridges [32,33] is driven by
104 intercellular differences in turgor pressure P , with a conductivity per unit surface L^s (Figure
105 1D). We assume water to move freely in the extracellular space (apoplasm), because available
106 data indicate that the apoplasm is not limiting water movement [34]. We did not prescribe
107 turgor pressure, instead letting it emerge from local mechanical and hydraulic interplays (see
108 STAR Methods for detailed model description).

109 We specified cell divisions using the recently introduced Willis-Refahi rule derived from
110 experimental data in the SAM: cells divide according to their size and size increment since
111 the previous division [35]. The simulations recreate distributions of neighbour number
112 (topological distributions) similar to those observed in the SAM (Figure 1G and 1H).

113 We set the model parameters based on classic measurements from Boyer [36] and Cosgrove
114 [37] (Table S1). We found turgor pressure to be heterogeneous, with a clear anticorrelation
115 with topology and with size: cells with fewer neighbours are smaller and have relatively
116 higher pressure (Figure 1K-1M, 3 simulations, cell number $n = 1535$, Pearson correlation
117 coefficient $R = -0.57$, $p < 10^{-100}$).

118 To test the robustness of model outputs, we explored its parameter space. Analytical
119 exploration in a two-cell system [30] had showed that system dynamics is mostly controlled
120 by three dimensionless parameters (see STAR Methods for details):

- 121 • α^s , which compares the balance between symplasmic and transmembrane water
122 conductivity ($1/2$ denotes equal contribution, $< 1/2$ transmembrane-predominance, $>$
123 $1/2$ symplasmic-predominance);

- 124 • α^a , which compares the balance of growth control by transmembrane water
125 conductivity and by cell wall extensibility (1/2 equal contribution, < 1/2 more control
126 by wall extensibility, > 1/2 more control by transmembrane conductivity); and
- 127 • θ , which assesses the osmotic drive of growth by comparing the cross-membrane
128 osmotic pressure difference and a representative threshold pressure for growth
129 (growth globally occurs when $\theta > 1$).

130 By varying values of α^s , α^a and θ in agreement with available measurements [36,37] (Table
131 S1) and allowing or arresting cell divisions, we recovered the turgor to size/neighbour-
132 number anticorrelation in all cases (Figure 1I-M, Figure 2A-K and Figure S2), demonstrating
133 that pressure heterogeneity is a robust behaviour of the model.

134 In simulations, like in SAM surface, cell neighbour number and size are coupled (Figure 1M,
135 2E, 2J, and 2K; Figure S2). Consistently, cell-specific turgor pressure anticorrelates with
136 normalized cell area (Figure 1L, 2D, 2I, and 2K; Figure S2). To uncouple cell size and
137 topology, we used three artificial templates, one with only hexagonal cells of varied sizes and
138 two with only square and octagonal cells. In the first case (constant topology), smaller cells
139 have higher pressure. In the latter cases, 4-neighbour cells always have higher pressure,
140 even with sizes similar to octagonal cells (Figure S1E-G). Altogether, turgor pressure
141 heterogeneity emerges independently from tissue topology and from cell size differences, as
142 further confirmed by an analytical prediction based on the Lockhart equation (Figure S1H-I).
143 Local topology determines cell wall angles and the subsequent tension distribution at each
144 tricellular junction (Figure 2L and 2M): in our model, wall stress and strain above the growth
145 threshold are relaxed at a rate limited by wall extensibility and hydraulic conductivity.
146 Therefore, in non-dividing simulations, stress and strain are homogeneous when water
147 movement is limiting for growth, and they remain relatively homogeneous when this
148 limitation is lifted (Figure 2F); then, the sum of wall tension at each tricellular junction
149 (vertex) mostly depends on the angles between walls. The vertex between three hexagonal
150 cells with 120° internal angles has a sum of tension at zero (Figure 2L). Fewer-neighbour
151 cells have sharper internal angles, so the sum of tension at vertex is greater towards the cell

152 interior, creating additional inward compression and prompting higher pressure build-up at
153 equilibrium (Figure 2M). In dividing simulations, new walls do not bear stress right after
154 division because they form from the cell interior. These new walls are gradually strained due
155 to mesh growth but do not yield (expand) to release stress before reaching the threshold
156 (Figure 1I and 2A). Consequently, cell division keeps the wall stress from homogenizing and
157 dampens the turgor–neighbour-number anticorrelation, compared to non-dividing simulations
158 (Figure 2C and 2H). In addition to its dependence on local topology, turgor pressure decreases
159 with cell size, similarly to the prescriptions of Laplace’s law.

160 Altogether, our results imply that local hydrostatic pressure heterogeneity does not require
161 differential cellular osmotic pressure [28] in a growing tissue, and predict a topological-and-
162 geometrical origin of pressure variability.

163 **Atomic force microscopy reveals heterogeneous turgor pressure in Arabidopsis shoot** 164 **apical meristem**

165 To test predictions, we built upon recent advances in atomic force microscopy (AFM) that
166 enabled non-invasive turgor pressure retrieval utilizing indentation force-displacement and
167 surface topography in living plant cells (Figure 3A) [38–42]. We used a pressurized thin-shell
168 model to deduce the turgor pressure value from the AFM-measured force-displacement
169 curves, which are influenced by turgor pressure, cell wall mechanical properties, cell 3D
170 geometry [38], and may reflect mechanical properties at different sub- to supra-cellular scales
171 according to indentation depths (Figure 3B-E). We applied AFM measurements to the
172 Arabidopsis SAM epidermis, a system featuring substantial growth heterogeneity (Figure 4A)
173 [1]. We included untreated soil-grown SAMs and a conceptually simpler model SAM co-
174 treated with naphthylphthalamic acid (NPA), a polar auxin transport inhibitor that induces
175 pin-formed SAMs, and oryzalin, a microtubule-depolymerizing drug that blocks cell division
176 but permits continuous, isotropic growth; hereafter referred to as “oryzalin-treated SAMs”
177 (Figure 4G) [28]. Walls between cells are often curved in growing oryzalin-treated SAMs,
178 suggesting that neighbouring cells have different turgor pressure [28] in a growing tissue.

179 Figure 3 illustrates the AFM measurement pipeline, where we determined SAM surface

180 topography with AFM (Figure 3F) and performed indentations near the cell centre to have
181 near-perpendicular indentation and minimize any bias due to surface slope (Figure 3G).
182 Physical values required to deduce pressure using the published theoretical formula [39,40],
183 except cell wall thickness separately measured by electron microscopy, are simultaneously
184 determined by AFM scan and indentation. Specifically, both mean curvature and Gaussian
185 curvature of outer cell walls directly contribute to the capacity to sustain turgor pressure
186 [38,39,43], and were determined from AFM scan topography (Figure 3F). As previously
187 suggested in tomato SAM [44], outer periclinal wall thickness is not very variable between or
188 within cells in Arabidopsis SAM, with untreated meristem $t_u = 179 \pm 7$ nm (mean \pm standard
189 error of mean, SEM) and oryzalin $t_o = 742 \pm 29$ nm (Figure S3A-D). Based on previous work
190 [45], we used indentation depths smaller than t_u to determine apparent Young's modulus of
191 cell wall (Figure 3B and 3E). We determined indentation stiffness, k , using depth ranges that
192 minimizes effect from cell wall and neighbouring cells to k (Figure 3C and 3E), so as to be in
193 the validity range of the pressurized shell model [40] (see STAR Methods for details). Finally,
194 we further validated our depth ranges using numerical simulations of indentations on realistic
195 3D meshes accounting for pressurized epidermal cells [46] (Figure 5; STAR Methods).

196 Cell-specific AFM indentations on seven untreated and nine oryzalin-treated SAMs revealed
197 that surface wall curvature, Young's moduli, cell apparent stiffness and the deduced turgor
198 pressure are all markedly heterogeneous across the SAM epidermis (Figure S3 and Figure 4).
199 We analysed intracellular and intercellular variability of all quantities measured, as well as the
200 sensitivity of deduced pressure, P , to variations in thickness (see STAR Methods for details).
201 All these indicate that P deduction is cell-specific, and that variability in cell wall mechanics
202 does not account for deduced pressure heterogeneity.

203 Based on AFM, we find that deduced turgor pressure is heterogeneous, with averages values
204 per meristem of 2.62 ± 0.03 MPa and 1.21 ± 0.11 MPa (mean \pm SEM) in untreated and
205 oryzalin-treated meristems, respectively (Figure S4A and S4J). As neither the classic pressure
206 probe nor the pico gauge [47] can be applied to cells as small as in the shoot apical meristem,
207 we assessed quantitatively the values of turgor pressure by using an incipient plasmolysis
208 assay to determine SAM osmotic pressure (see STAR Methods). We found that untreated

209 SAMs have osmotic pressure between 1.0 and 1.5 MPa, while oryzalin-treated SAMs range
210 from 1.5 to 2.4 MPa based on the threshold for plasmolysis (Figure S5, STAR Methods), with
211 no obvious cell-to-cell heterogeneity in plasmolysis threshold. Altogether, the values of turgor
212 found with AFM are in semi-quantitative agreement with the values of osmotic pressure
213 deduced from incipient plasmolysis (see STAR Methods for a discussion of the discrepancy).

214 **Cell pressure in shoot apical meristem anticorrelates with local topology and size**

215 Next, we tested model predictions and found that AFM-determined cellular pressure of
216 untreated SAM, normalized to the average value per meristem, anticorrelates with the number
217 of epidermal cell-neighbours N , or local topology (7 SAMs, $n = 503$ cells, $R = -0.16$, $p = 10^{-4}$,
218 Figure 4E; see also Figure S4A for absolute pressure values). Given the linear relationship
219 between cell area and neighbour number (Figure 4C) due to fundamental geometrical
220 constraints in compact tissues [48], normalized pressure was also correlated with cell size A
221 ($R = -0.23$, $p = 10^{-7}$, Figure 4F).

222 Encased in rigid cell walls, plant cells seldom exchange neighbours, and the main source of
223 topological change is via division, where dividing cells tend to lose neighbours and cells
224 adjacent to the division plain tend to gain neighbours [49]. We therefore considered oryzalin-
225 treated SAM, in which cell divisions are arrested while growth is continuous, and recovered
226 similar anticorrelation for normalized pressure against neighbour number (9 SAMs, $n = 202$
227 cells, $R = -0.32$, $p = 10^{-6}$) and against cell area ($R = -0.35$, $p = 10^{-7}$) (Figure 4K and 4L; also
228 see Figure S4 for absolute values).

229 We then examined whether such trends may be caused by trends in cell wall thickness, t , or
230 modulus, E , or by trends in stiffness, k (STAR Methods; Figures S3 and S4). None of these
231 mechanical parameters could explain P heterogeneity. Moreover, we found that turgor
232 pressure heterogeneity may be removed when sample is osmotically challenged: the same
233 SAM shows heterogeneous pressure when turgid and homogeneous pressure when at
234 intermediate turgidity (Figure S5B). Altogether, the AFM approach is not technically biased
235 by tissue topology and/or cell size in determining cell-to-cell variations in pressure.

236 Finally, we used cell side wall convexity as a proxy for differences in turgor, because cells
237 with higher pressure would be expected to bulge out into cells with lower pressure (Figure
238 S4O) [50]. We constructed a weighed convexity index (wCI) (Figure S4F), and found that
239 convexity significantly anticorrelates with number of neighbours, in agreement with
240 qualitative observations in oryzalin-treated meristems [28], as well as with turgor pressure
241 (Figure S4G and S4P).

242 Altogether, our data indicate that non-random turgor pressure heterogeneity establishes in
243 tissues with static topology (no neighbour number change) or dynamic topology (neighbour
244 numbers change due to division). Although tissue topology and cell size are sufficient to
245 explain pressure heterogeneity, we do not exclude a role of other biological parameters and/or
246 sources of noise in pressure variations, as suggested by weaker correlations in experiments
247 (Figure 4) than in simulations (Figure 1 and 2).

248 **Realistic mechanical models of tissue indentation support pressure heterogeneity**

249 Whereas the aforementioned pressure deduction is based on a model utilizing local cell shape
250 [39], cell packing may also contribute to the indentation stiffness [46]. We therefore
251 implemented realistic indentation using a membrane indentation finite element method (FEM)
252 model following Mosca et al. [46]. We first constructed an epidermal realistic template from
253 the confocal image and thickness measurements of the untreated SAM displayed in Figure 4A
254 (see STAR Methods, Figure 5A and 5B), inflated it by uniform turgor pressure (2 MPa,
255 rounded from experimental values) as the null hypothesis, and performed indentations on the
256 exact corresponding cells indented experimentally, excluding cells at template periphery to
257 avoid boundary effects. We noticed that deep indentation of 2 μm deforms both the indented
258 and its neighbouring cells (Figure 5E to 5G), representing supracellular measurement (Figure
259 3D) and potentially explains the effect of cell packing on indentation stiffness [46]. We
260 therefore implemented the same indentation depth range from experiments for cell-specific
261 readout (see STAR Methods), and recovered comparable values of apparent stiffness k for the
262 untreated-like template $k_{\text{FEM}} = 14.9 \pm 0.2$ N/m (mean \pm SEM, compared to $k_{\text{AFM}} = 12.9 \pm 0.2$
263 N/m). However, cell-specific k differs from experiment, and the trend of measured and

264 simulated k is reverted (Figure 5H). We then discarded the null hypothesis and prescribed
265 heterogeneous pressure based on the values found experimentally (see STAR Methods).
266 Introducing cell-specific turgor pressure in untreated-like template successfully corrected the
267 distribution of indentation stiffness (Figure 5J) and statistically improved correlation of
268 curvature, another quantity directly linked to P (Figure 5I and 5K). Similarly, indentations on
269 the template based on the oryzalin-treated SAM in Figure 4G recovered indentation stiffness
270 on the same magnitude of experiment values ($k_{\text{FEM}} = 38.7 \pm 0.9$ N/m, compared to $k_{\text{AFM}} = 14.5$
271 ± 0.6 N/m), and implementing variable pressure also improved agreements between simulated
272 and experimentally measured stiffness (Figure 5L and 5N). We note however that FEM
273 simulations do not recapitulate curvature of treated SAM (Figure 5M and 5O), implying that
274 an additional hypothesis would be needed to account for curvature variability in this case.
275 Altogether, these results indicate that the contribution of cell packing to the measured
276 variability is negligible with our indentation depths and suggest that AFM-measured
277 variability captures the main component of non-random pressure heterogeneity.

278 **Two types of correlations between cell growth and local topology or size**

279 Next, we monitored areal growth rate of SAM epidermal cells by time-lapse confocal
280 microscopy. As observed previously, untreated SAMs exhibited slower growth in the centre,
281 where stem cells reside, than the surrounding cells [51] (Figure S6D). Additionally, cellular
282 growth rate anticorrelates with neighbour number (11 SAMs, $n = 1491$ cells, $R = -0.15$, $p =$
283 10^{-8} ; Figure 6E) and cell size ($R = -0.33$, $p = 10^{-38}$; Figure 6F), supporting previous reports
284 that smaller cells in SAM grow faster [35,52], and suggesting that higher turgor pressure in
285 fewer-neighboured cells associates with faster growth. In oryzalin-treated SAMs, however,
286 the fewer-neighboured and small cells grew slower (14 SAMs, $n = 1160$ cells; neighbour
287 number $R = 0.20$, $p = 10^{-11}$, Figure 6K; cell size $R = 0.16$, $p = 10^{-8}$, Figure 6L). This suggests
288 that higher turgor pressure associates with either faster or slower growth depending on
289 conditions. Although seemingly a small shift, this negative-to-positive slope change of local
290 growth heterogeneity captures a strong qualitative inversion of growth behaviour (Figure 6D
291 and 6J). Accordingly, smaller cells expand more than larger cells in untreated SAMs, which
292 may contribute to cell size homeostasis, a phenomenon that would be absent in oryzalin-

293 treated SAMs.

294 **Heterogeneity in growth rate is patterned according to the balance between wall**
295 **extensibility, tissue conductivity, and osmotic drive**

296 We further explored the growth trend in our vertex model. Based on the parameter exploration
297 on dividing mesh aimed to reproduce untreated SAM behaviour, we found that some
298 parameter sets predict negative correlation between growth rate and cell neighbour number,
299 while others predict positive correlation (Figure 7 and Figure S7). This indicates that growth
300 trend is sensitive to the balance between water flux and wall expansion (governed by the non-
301 dimensional parameter α^a , see STAR Methods) and by the osmotic drive (ratio of osmotic
302 pressure to yield pressure, $\theta = \Delta\Pi/P^Y$). This can be rationalized by examining the relative
303 growth rate G of an isolated cell according to the Lockhart model (see [30])

304
$$G = 1/2 (\alpha^a \Phi^w h/w) (\Delta\Pi - P^Y),$$

305 in which we allow both α^a and P^Y to vary with the surface to volume ratio: hence, both the
306 prefactor $\alpha^a \Phi^w h/w$ and the yield pressure P^Y decrease with cell size R and neighbour
307 number N , while $\Delta\Pi$ is constant. Consequently, two regimes are expected: when the osmotic
308 drive θ is smaller than a threshold θ^T , G is dominated by the variations of P^Y , therefore G
309 increases with cell size and with neighbour number, which corresponds to the trend in
310 oryzalin-treated meristems; when $\theta > \theta^T$, the variations of P^Y are negligible, so G follows
311 the prefactor and decreases with cell size, which corresponds to the trend in untreated
312 meristems. These two regimes occur whatever the value of α^a , and the threshold value θ^T
313 increases with increasing α^a .

314 In the vertex model, many global parameter shifts can invert growth trend through changes in
315 these dimensionless parameters (Figure 7K and 7L; Figure S7). The model retrieves untreated
316 SAM trends if transmembrane conductivity partially limits growth (α^a not too large),
317 symplasmic conductivity is not on par with transmembrane conductivity (α^s not too large), or
318 if the osmotic drive θ is sufficiently large. Conservatively, we chose equal contribution by
319 flux and wall in our model ($\alpha^a = 0.5$), and increased osmotic pressure to 2 MPa, a value

320 comparable to the experimental measurements: Figures 7A-C show that the fewer-
321 neighboured and smaller cells grow faster (3 simulations, $n = 1496$; G vs N , $R = -0.10$, $p = 10^{-4}$;
322 G vs A , $R = -0.76$, $p < 10^{-100}$).

323 We then attempted to reproduce oryzalin-treated behaviour, guided by the experimental
324 observations that, besides stopping cell division, oryzalin treatment also yields higher osmotic
325 pressure (1.6-fold) and drastically thicker cell walls (4-fold) (Figure S3 and S5). We found
326 that both stalling division and increasing osmotic pressure failed to invert the growth trend in
327 the model, as expected, while doubling and quadrupling wall thickness inverted the
328 correlation of growth rate to neighbour number and cell size (Figure 7D-J and Figure S7), like
329 in oryzalin-treated SAM. Combining higher osmotic pressure and thicker wall revealed that
330 quadrupling wall thickness can robustly trigger growth trend inversion (Figure 7J and Figure
331 S7).

332 Effectively, changing osmotic pressure and wall thickness alter the wall-flux limitation
333 balance of the system (Figure 7J-L). Higher osmotic pressure induces faster water influx
334 (reduced limitation by hydraulics). The extra volume strains the walls to accumulate stress
335 farther beyond the threshold, which is relaxed by wall yielding (growth) with extensibility as
336 the rate limit. Meanwhile, wall thickening reduces wall stress and strain towards the threshold
337 for expansion, effectively reducing the mechanical drive of growth and increasing the weight
338 of water permeability in limiting growth. We do not exclude other possible parameter changes
339 triggered by oryzalin treatment, like water conductivity and wall synthesis rate, that would
340 also contribute to the wall-flux limitation balance. Nevertheless, implementing the observed
341 cell wall thickening in the model is sufficient to explain the observed growth rate inversion
342 from untreated to oryzalin-treated scenario.

343 **DISCUSSION**

344 In this study, we modelled the growth of a plant tissue by coupling tissue mechanics and
345 tissue hydraulics. This generalizes previous models focusing only on mechanics [53–55]. In
346 this model, both cell growth and turgor pressure emerge from mechanics and hydraulics. Each
347 of these parameters can be controlled by genetic and biochemical inputs, and small uniform

348 changes in these biological inputs can enable drastic shifts of system behaviour and the final
349 cell size distribution. We predicted that a broad distribution of neighbour number leads to
350 heterogeneity in cell growth and in turgor pressure, even when hydraulics has a minor
351 contribution to the control of growth. We verified this prediction in the context of the shoot
352 apical meristem (SAM) of *Arabidopsis thaliana*. In the model, we assumed osmotic pressure
353 to be homogeneous and heterogenous turgor pressure emerges from model dynamics. In the
354 SAM, we cannot exclude that heterogenous osmotic pressure contributes to heterogeneous
355 turgor; however, it is unlikely that osmotic pressure is highly heterogeneous based on the
356 incipient plasmolysis assay; furthermore, two modes of osmoregulation would be required to
357 account for the different growth trends in untreated and oryzalin-treated SAM. It remains to
358 be seen whether our results apply to other plant or animal tissues, or this is specific to the
359 SAM. Finally, to make the model tractable, we assumed apoplastic water movement to be
360 non-limiting and we neglected the mechanics of periclinal walls and of underlying cells.
361 Further work should lift these assumptions, though they should not affect any of the
362 qualitative trends found here [56].

363 To test our predictions and deduce pressure in the SAM, we combined a recently developed
364 indentation-based approach [40] with FEM-based realistic mechanical models of indentation
365 [46]. We found values of turgor in the range 1-3 MPa range, higher than the range 0.2-1 MPa
366 typically measured in plant tissues [18], though values of up to 5 MPa were measured in
367 guard cells [57]. For instance, the *Arabidopsis* root epidermis has a turgor of about 0.4 MPa,
368 as measured with the pressure probe [58]; the *Arabidopsis* leaf epidermis has a turgor of about
369 1-2 MPa, as deduced from indentation and mechanical modelling [59]. Accordingly, we
370 speculate that the SAM function might require relatively high turgor. Another specificity of
371 the SAM could be a relatively low transmembrane conductivity, as most aquaporin (channel
372 protein allowing rapid transmembrane water flux [34]) isoforms had significantly lower
373 expression in inflorescence than in other fast growing tissues like stem and root [60] (with a
374 reduction up to ~80%). Nevertheless, a wide range of water conductivity can produce
375 pressure heterogeneity, including very high conductivity (i.e. $\alpha^a = 0.9$ [37]), and the
376 agreement between model predictions and experimental measurements suggests that tissue

377 hydraulics has a (possibly small) contribution to limiting growth in the SAM. Interestingly,
378 altered expression of the aquaporin PIP2;1 delays the emergence of lateral roots [61], also
379 hinting to a developmental role for hydraulic conductivity. Altogether, we propose that tissue
380 mechanics and hydraulics act in concert with the established genetic regulations in SAM cell
381 growth.

382 We found that both cell growth and turgor pressure are heterogeneous in the SAM. It has
383 already been reported that smaller cells [52] or the smaller of two sister cells [35] grow faster
384 in the SAM of untreated and NPA-treated plants, respectively. We found the same trend in
385 untreated SAM, with an inversion in oryzalin-treated SAM. Such inversion is relevant to
386 normal development: for example, it occurs in cell clones during sepal development,
387 effectively shifting from homogenizing to amplifying cell size variability [62]. In untreated
388 SAM, small cells grow faster than big cells, possibly contributing to tissue homeostasis.
389 Finally, irrespective of the conditions, we find that turgor pressure is smaller in big cells in
390 experiments, which might contribute to reducing mechanical stress in the cell wall in these
391 cells [63]; this would act in parallel with the mechanism proposed in the context of leaf
392 epidermal cells, based on cells adopting puzzle shapes that limit cell wall stress [63].

393 Our results point towards a link from cell topology (number of neighbours) and geometry to
394 cell mechanical status. This might also be relevant to animal epithelia [29], though this
395 appears unexplored experimentally. Feedbacks from cell mechanics to cell topology are more
396 established: cell division and thus number of neighbours can be oriented by mechanical stress
397 in animals and in plants [64–67]. Since tissue topology is highly conserved in many biological
398 systems [68], we propose that pressure heterogeneity may emerge in compact tissues with
399 polygonal cells [61] and non-instantaneous water movement, due to the adjustment to
400 reconcile local mechanical and hydraulic conditions.

401 Finally, we note that heterogeneous patterns may not always be stochastic [69]. The emergent
402 heterogeneity of local growth and hydrostatic pressure is coupled with the characteristic yet
403 dynamic tissue topology [48,49], all based on stringent rules and likely underlies
404 morphogenesis in compact tissues. With the discovery of many cell-size-dependent transcripts

405 [3,70], our model proposes another source for non-random variability in a tissue.

406

407 **Acknowledgements**

408 We thank P. Bolland and A. Lacroix for plant care, G. Cloarec for help with TEM, L.
409 Beauzamy for AFM training, C. Mollier for help in estimating confocal technical errors, G.
410 Cerutti for help in implementing the division algorithm and in segmentation, S. Strauss for
411 help in mesh format conversion, R. Smith for help in segmentation and mesh generation for
412 the indentation simulations, and V. Battu, F. Zhao and C. Galvan-Ampudia for providing plant
413 materials. We acknowledge the contribution of the PLATIM facility of SFR Biosciences
414 (UMS3444/CNRS, US8/Inserm, ENS de Lyon, UCBL) for AFM and confocal microscopy,
415 and of Centre Technologique des Microstructures (UCBL, Lyon) for electron microscopy.
416 This work was supported by a fellowship from Institut Universitaire de France, an ERC
417 Starting Grant to A.B. (ERC-2012-StG-307387) and a scientific award from the Simone and
418 Cino Del Duca foundation to A.B., an EMBO Long-term Fellowship to Y.L. (EMBO ALTF
419 168-2015), an Agropolis Foundation grant (MecaFruit3D) to I.C. and C.G, and a
420 Forschungskredit Fellowship awarded by the University of Zurich (K-74502-04-01) to G.M.

421

422 **Author contributions**

423 This study was initiated by A.B. Y.L. and A.B. designed the experiments. Y.L. executed AFM
424 and confocal microscopy, acquired experimental data except electron microscopy, and
425 analysed experimental and simulation data. J.T. performed electron microscopy. V.M, M.D.
426 and A.K. wrote scripts to facilitate experimental data analysis. I.C. and C.G. designed
427 physical model of tissue growth. I.C. implemented the model, ran simulations, optimized
428 model parameters and analysed simulation data. G.M. designed, ran, and analysed indentation
429 simulations. Y.L. and A.B. contributed to the design of simulations. Y.L., I.C., V.M., G.M.,
430 C.G. and A.B. contributed to data interpretation. Y.L. and A.B. wrote the manuscript with
431 inputs from the other authors.

432

433 **Declaration of Interests**

434 The authors declare no competing interests.

435 **MAIN FIGURE TITLES AND LEGENDS**

436

437 **Figure 1. Turgor pressure heterogeneity emerges from cell topology and cell size in a**
438 **mechano-hydraulic model.**

439 (A) In a plant cell, the turgor pressure P is contained by the cell wall tensile stress σ . (B) A
440 schematic representation of the Lockhart-Ortega equation, where 1D cell length L elongation
441 is a combination of reversible stretch εL (elasticity, ε is elastic strain) and cell wall yield ΔL
442 at longer timescale (viscosity) if P is higher than a threshold P^Y (effective plasticity, $\Delta L = \Phi t$
443 $L (P - P^Y)$, Φ is wall extensibility, t is time). (C to F) Schematic representations of model
444 components, including cell geometry with height h and typical radius R (C),
445 apoplasmic/transmembrane and symplasmic/intercellular water fluxes (D), mechanical
446 equilibrium at tricellular junctions (E) and the visco-elasto-plastic cell wall rheology (F). P_i ,
447 cell-specific turgor pressure; σ , cell wall tension; Φ^w , wall extensibility; ε^Y , wall strain
448 threshold; E , wall Young's modulus. (G) Simulation snapshots: in “dividing” simulations, 16
449 initial cells grow and divide until about 600 cells; in “non-dividing” simulations, divisions are
450 stopped when cell number reaches about 300 and growth continues until they triple in size.
451 Colour indicates cell neighbour number as in (H). (H) Similar distributions of cell neighbour
452 number in the experimentally observed (Exp.) shoot apical meristem and in simulations
453 (Sim.) by Kolmogorov–Smirnov test (confidence level $\alpha = 0.05$, $D_{n,m} < D_\alpha$), error bars are
454 standard deviations. *, Student's t -test $p < 0.05$; **, $p < 0.01$. (I-M) Cell wall strain, turgor
455 pressure, neighbour number, and area in dividing simulations; growth was assumed to be
456 limited by both cell wall and transmembrane water movement (dimensionless parameter for
457 flux-wall balance $\alpha^a=1/2$) ([71], Table S1), transmembrane and cell-to-cell conductivity are
458 assumed equal (dimensionless parameter for apoplasmic-symplasmic balance, $\alpha^s=1/2$), and
459 the ratio of osmotic pressure yield pressure to yield pressure is taken from literature
460 (dimensionless osmotic drive, θ) ([71], Table S1). (I to J) Example of simulation output: cell
461 wall elastic strain ε normalized by yield strain ε^Y (I); cell turgor pressure P normalized by
462 average pressure (J). (K to M) Boxplots (1535 cells) of normalized cellular turgor pressure P
463 against cell neighbour number N (K); normalized pressure against normalized area A (L);
464 normalized area A against neighbour number N (M). Cells on the mesh edge were not

465 analysed to avoid border effect. Circles are Tukey's outliers; lowercase letters indicate
466 statistically different populations (Student's t -test, $p < 0.05$); red lines indicate linear
467 regressions, with Pearson correlation coefficient R and corresponding p -value. In (G and I)
468 scale bars are 5 unit length.

469 See also Figure S1, Table S1, and Data S1.

470

471 **Figure 2. Turgor pressure heterogeneity is robust to model parameters.**

472 (A to J) Cell wall strain, turgor pressure, neighbour number, and area in dividing (A to E) and
473 non-dividing (F to J) reference simulations; the dimensionless parameters for limitation of
474 growth by cell wall or by transmembrane water movement α^a , for balance of cell-to-cell and
475 transmembrane hydraulic conductivity α^s , and the osmotic drive θ (ratio of osmotic to yield
476 pressure) are as indicated. (A and F) cell wall elastic strain ε normalized by yield strain ε^Y
477 (scale bars are 5 unit length); (B and G) cell turgor pressure P normalized by average
478 pressure; (C and H) middle: boxplots of normalized cellular turgor pressure P against cell
479 topology N (C-E, $n = 1496$ cells; H-J, $n = 759$ cells); (D and I) normalized pressure against
480 normalized area; (E and J) normalized area against neighbour number. Cells on the mesh edge
481 were not analysed to avoid border effect. Circles are Tukey's outliers; lowercase letters
482 indicate statistically different populations (Student's t -test, $p < 0.05$); red lines indicate linear
483 regressions, with Pearson correlation coefficient R and corresponding p -value. (K) Model
484 parameter exploration. Colours indicate Pearson correlation coefficient R , with perfect
485 anticorrelation as blue ($R = -1$), perfect correlation in red ($R = 1$); all correlations were
486 statistically significant ($p < 0.05$). A , normalized cell area; N , cell neighbour number; P ,
487 normalized turgor pressure; α^a , dimensionless parameter for flux-wall balance; α^s ,
488 dimensionless parameter for apoplasmic-sytoplasmic balance; θ , dimensionless osmotic drive.
489 (L and M) Schematic explanation of topology-derived turgor pressure heterogeneity. (L)
490 Tricellular junctions in a tissue of hexagonal cells are at mechanical equilibrium with equal
491 tensions and equal wall-wall angles. (M) Fewer-neighbour cells have sharper wall-wall
492 angles, a tension that is roughly constant per wall effectively results in mechanical
493 compression due to unequal projected tension distribution (red dash-line arrow) that is
494 balanced by higher turgor pressure build-up (big blue arrow).

495 See also Figure S1, Figure S2, Table S1, and Data S1.

496

497 **Figure 3. The experimental pipeline for turgor pressure deduction.**

498 (A) Schematic representation of AFM nanoindentation for turgor pressure measurement. r ,
499 probe tip radius; k , cantilever stiffness. (B to E) Illustration for force curve interpretation at
500 different indentation depth, Z . (B) When indentation depth Z_1 is smaller than wall thickness t ,
501 the force-indentation curve is sensitive to cell wall property, (C) deeper-than-wall indentation
502 $Z_2 > t$ is also sensitive to turgor pressure P . (D) Even deeper indentation Z_3 deforms
503 surrounding cells and is also sensitive to tissue context. Dotted line marks the shell position
504 before indentation, which is used to determine surface mean and Gaussian curvature, κ_M and
505 κ_G , by AFM topographic scan. (E) Three regimes of the force-indentation curve are used to fit
506 for cell wall Young's modulus E (a measure of wall elasticity), apparent stiffness at cell-scale
507 k_s and tissue scale k_d . F denotes indentation force. (F to L) The AFM-confocal pipeline of
508 measurement and deduction on an example untreated SAM. (F) Derjaguin-Muller-Toporov
509 (DMT) modulus map, highlighting cell contours, is projected on the surface topography of an
510 AFM scan. Smaller scan region is chosen to bypass the SAM surface unevenness. (G)
511 Multiple indentations (marked by crosshair) are performed near the barycentre of each cell.
512 (H and I) Confocal stack and its surface projection of the same SAM with plasma membrane
513 GFP signal. (J) Tiled AFM scans are overlaid and stitched on the confocal surface projection
514 image, red square marking the same tile from (G). Individual indentation positions are
515 registered on a global coordinate and assigned to segmented cells. (K) Force curves are
516 analysed, and the cellular average of physical values are mapped. (L) Turgor pressure is
517 deduced per force curve and averaged per cell. Stiffness from very deep indentation is not
518 used for cell-specific deduction.

519 See also Figure S3, STAR Methods, and Data S2.

520

521 **Figure 4. Turgor pressure heterogeneity in untreated and oryzalin-treated SAM.**

522 Turgor pressure, topology, and cell area in untreated (A to F; 7 SAMs, $n = 503$ cells) and
523 oryzalin-treated SAM (G to L; 9 SAMs, $n = 202$ cells). (A and G) Top-view surface
524 projections of untreated SAM with plasma membrane GFP signal; scale bars represent $20 \mu\text{m}$.

525 (B and H) Map of epidermal cell neighbour number (same SAMs as in A and G, respectively).
526 (C and I) Normalized cell area A and cell neighbour number N are linearly correlated. (D and
527 J) Map of AFM-determined turgor pressure (same SAMs as in A and G, respectively). (E-F
528 and K-L) Association of turgor pressure, P , with neighbour number N and cell area A , all
529 plotted values are normalized per SAM.
530 See also Figure S4, Figure S5, and Data S2.

531

532 **Figure 5. A membrane indentation finite element method (FEM) applied to realistic**
533 **templates supports the deduction of pressure heterogeneity.**

534 (A to G) Virtual indentation on realistic 3D mesh. (A and B) The epidermal layer of the
535 example untreated meristem in Figure 4 is meshed based on confocal image. Cells are
536 pressurized with a uniform 2 MPa turgor pressure. (C and D) A cell before (red) and being
537 indented (magenta). (E to G) Longitudinal section of the indented mesh; black, before
538 indentation; magenta, being indented. Cell junctions (rectangles) are magnified to highlight
539 the neighbour cell deformation (marked by asterisks) by very deep indentation. Scale bars are
540 as specified. (H to K) Plots of normalized values of AFM-measured indentation stiffness k
541 and cell surface curvature κ_M against FEM-determined ones from meshes with uniform
542 pressure of 2 MPa. Both meshes are based on the example meristems in Figure 4. (L to O)
543 Plots of AFM-measured k and κ_M against FEM-determined ones from meshes with variable
544 pressure based on AFM deductions. Note the negative-to-positive switch between measured
545 and simulated k in untreated meristem (H and L) and the generally improved correlations in
546 simulations with variable pressure. Untreated-like $n = 20$ cells, oryzalin-treated like $n = 12$
547 cells. Red lines indicate linear regressions, with Pearson correlation coefficient R and
548 corresponding p -value.

549 See also Table S2 and Data S3.

550

551 **Figure 6. Cellular growth rate bifurcates between conditions.**

552 (A to F) Relative growth rate per day G of untreated SAM cells. (G to L) Cellular growth rate
553 per day of oryzalin-treated SAM between 12-hour interval (48 and 60 hours post treatment).
554 (A, B, G and H) Surface projections of untreated or oryzalin-treated SAM at initial time point

555 (A and G) and 12 hours later (B and H); scale bars are 20 μm unless otherwise noted. (C and
556 D) Heat maps of areal relative growth rate per day. (D and J) Example 4 and 8-neighbored
557 cells during 24-hour growth, with areal normalization at initial time point. Cell contour and
558 relative size (blue for 4-neighbored, red for 8-neighbored) depict the diverging growth trends.
559 Scale bars are as indicated. (E, F, K and L) Box plots of relative growth rate per day G against
560 cell topology N (E and K) and dot plots of relative growth rate per day G against normalized
561 cell area A (F and L) (E and F, untreated 11 SAMs, $n = 1491$ cells; K and L, oryzalin-treated
562 14 SAMs, $n = 1160$ cells). Note that Tukey's outliers are plotted in Figure S6 and all data are
563 included for statistical analyses. Lowercase letters indicate statistically different populations
564 (Student's t -test, $p < 0.05$); red lines indicate linear regressions, with Pearson correlation
565 coefficient R and corresponding p -value.

566 See also Figure S6 and Data S2.

567

568 **Figure 7. The model recapitulates the untreated and oryzalin-treated growth trends.**

569 (A to I) Relative growth rate G normalized by average growth rate, neighbour number N , and
570 normalized cell area A , with reference values of dimensionless parameters ($\alpha^a = 0.5$, $\alpha^s = 0.5$,
571 $\theta = 20/3$): dividing simulations (A to C), non-dividing simulations (D to F), and non-dividing
572 simulations with quadruple wall thickness w to mimic oryzalin treatment (G to I). (A, D, G)
573 Heat maps of normalized areal relative growth rate. (B, E, H) Box plots of normalized relative
574 growth rate G against cell topology N . Lowercase letters indicate statistically different
575 populations (Student's t -test, $p < 0.05$); red lines indicate linear regressions, with Pearson
576 correlation coefficient R and corresponding p -value. (C, F, I) Dot plots of normalized relative
577 growth rate G against normalized cell area A . For numbers of repeats see STAR Methods. (J)
578 Model exploration to fit oryzalin-treated case. Colours indicate Pearson correlation R , with
579 perfect anticorrelation as blue ($R = -1$), perfect correlation in red ($R = 1$), and insignificant
580 correlation ($p > 0.05$) in black. A , normalized cell area; N , cell neighbour number; P ,
581 normalized turgor pressure; G , normalized relative growth rate; $\Delta\Pi$, transmembrane osmotic
582 pressure difference; w , wall thickness. (K and L) Influence of dimensionless (K) and
583 dimensional parameters (L) on growth trends. Triangles indicate parameter's influence to the
584 mechanical-hydraulic balance. α^a , dimensionless parameter for flux-wall balance; α^s ,

585 dimensionless parameter for symplasmic-apoplasmic balance; θ , dimensionless osmotic drive.
586 w , wall thickness; E , cell wall modulus; ε^Y , strain threshold; L^a , cross-membrane water
587 conductivity; L^s , cell-to-cell symplasmic conductivity; Φ^w , wall extensibility; $\Delta\Pi$,
588 transmembrane osmotic pressure difference; R , representative cell size.
589 See also Figure S7, Table S3, and Data S1.
590

591 **STAR Methods**

592

593 **LEAD CONTACT AND MATERIALS AVAILABILITY**

594 All materials, scripts and datasets generated and analysed during the current study are
595 available from the Lead Contact, Arezki Boudaoud (arezki.boudaoud@ens-lyon.fr). This
596 study did not generate new unique reagents.

597

598 **EXPERIMENTAL MODEL AND SUBJECT DETAILS**

599 **Plant material and growth conditions**

600 *Arabidopsis thaliana* *GFP-LTi6b* (ecotype WS-4) reporter line [72], wild-type, *DR5::Venus*
601 reporter line [73] and *PINI-GFP* reporter line [74] (ecotype Col-0) were used (see Key
602 Resources Table and Supplemental Excel Table 2, 3, 5 and 6). Untreated inflorescence
603 meristems were obtained from soil-grown plants, first in short-day (8 h light 20°C / 16 h dark
604 19°C cycle) for 3 to 4 weeks then transferred to long-day (16 h light 20°C / 8 h dark 19°C
605 cycle) for 1 to 2 weeks to synchronize bolting.

606

607 **METHOD DETAILS**

608 **Plant treatments**

609 Oryzalin-treated inflorescence meristems were obtained from plants grown on custom-made
610 *Arabidopsis* medium [75] (Duchefa) supplemented with 1% agar-agar (Merck) and 10 µM N-
611 1-naphthylphthalamic acid (NPA, Sigma-Aldrich/Merck) for 3 weeks. Pin-formed
612 inflorescence meristems from NPA medium were immersed in 10 µg/mL oryzalin (Sigma-
613 Aldrich/Merck) twice (3 h duration, 24 h interval) [28]. For mechanical measurements and
614 time-lapse confocal imaging, meristems were mounted on *Arabidopsis* apex culture medium
615 (ACM) [75] with 2% agarose and 0.1% plant preservation mixture (PPM, Plant Cell
616 Technology) to prevent contamination, and cultivated in long-day condition.

617 **Atomic force microscopy**

618 Untreated meristems (dissected, with most late stage-2 floral primordia removed to prevent
619 blocking of the cantilever) and oryzalin-treated meristems were mounted on ACM (2%
620 agarose, 0.1% PPM) the night before. Drops of 2% low melting agarose (Duchefa) were
621 applied around the lower parts of meristems for mechanical stabilization. For oryzalin-treated
622 meristems, 72 h post-treatment meristems were measured.

623 AFM indentations were performed as in Beauzamy et al., 2015 [40]. Specifically, a BioScope
624 Catalyst model AFM (Bruker) operated with the NanoScope software (version 9.1, Bruker),
625 under a MacroFluo optical epifluorescence microscope (Leica), was used. All measurements
626 were done with customized 0.8 μm diameter spherical probes mounted on silicon cantilevers
627 of 42 N/m spring constant (SD-Sphere-NCH-S-10, Nanosensors). Cantilever deflection
628 sensitivity was calibrated against a clean sapphire wafer submerged in water before each
629 session.

630 Meristems were submerged in water during AFM measurements. PeakForce QNM mode was
631 used to record sample surface topography and cell contours (aided by the stiffness difference
632 between periclinal and anticlinal cell walls on DMT modulus maps) in overlapping square
633 tiles of 30 \times 30 to 50 \times 50 μm^2 (128 \times 128 pixels). Force curves were obtained by the point-and-
634 shoot mode of the NanoScope software, with at least 3 locations chosen near the barycentre of
635 each cell, and 3 consecutive indentations per location, making at least 9 force curves per cell.
636 Approximately 10 μN maximum force was applied during each indentation, corresponding to
637 approximately 1 μm indentation depth.

638 For hyperosmotic treatments, oryzalin-treated meristems were mounted in Petri-dishes on
639 Patafix (UHU), then the gap between Patafix and sample base was quickly sealed with bio-
640 compatible glue Reprorubber-Thin Pour (Flexbar) for stabilization. After the glue solidified
641 (less than 2 minutes), samples were submerged in liquid ACM containing 0.1% PPM.
642 Samples were first measured in liquid ACM (plus 0.1% PPM), then submersion medium was
643 changed to ACM plus desired concentration of NaCl (plus 0.1% PPM) by first rinsing with
644 3~5 mL target solution, then soaked in target solution for 5 minutes before AFM

645 measurements. Each new measurement per solution change took around 30 minutes.

646

647 **Electron microscopy**

648 For serial block-face imaging SEM (SBF-SEM), plants were grown in vitro on medium
649 containing the auxin transport inhibitor NPA (Naphtalene Phtalamic Acid) to generate stems
650 with naked meristems and were locally treated for 48h with the microtubule depolymerizing
651 drug oryzalin (Sigma) in lanolin at a concentration of 2 $\mu\text{g}/\mu\text{l}$ [76]. These plantlets were
652 subsequently taken off the inhibitor and left to regenerate for 48h on normal Arabidopsis
653 medium. Meristems with young organ primordia were fixed in 0.5% glutaraldehyde (in
654 demineralized water), from 25% Sigma stock in Microscopy Facility lab. The plantlets were
655 left at room temp for 2h in an Eppendorf and rinsed 1x in water before post fixation and de-
656 hydrating and embedding in Spurr's epoxy as described in [77]. The samples were then
657 sectioned and viewed in a Zeiss Merlin SEM [77].

658 For standard transmission electron microscopy fixed meristems of soil grown plants were
659 embedded in Spurr's resin and sectioned before viewing in a Jeol 2100F (at the Centre
660 Technologique des Microstructures, UCBL, Lyon).

661

662 **Time-lapse confocal microscopy**

663 Untreated (dissected) and oryzalin-treated meristems were mounted and grown on ACM with
664 0.8% agarose and 0.1% PPM for live imaging. Confocal stacks were taken on an LSM 700
665 confocal microscope (Carl Zeiss) operated with the ZEN 2010 software (version 6.0, Carl
666 Zeiss), using a W N-Achroplan 40x/0.75 M27 water immersion objective, and on a TCS SP8
667 confocal microscope (Leica) operated with the Leica Application Suite X software (version
668 3.5, Leica), using a Fluotar VISIR 25x/0.95 water immersion lens. GFP was excited at 488
669 nm and emission detected between 415 – 735 nm. Stacks have resolution of 1028×1028
670 pixels, with resolution ranging between 3.2 to 4.4 pixels/ μm ; Z steps were between 0.5 and
671 0.85 μm .

672 For hyperosmotic treatments, meristems were mounted in Petri-dishes on Patafix (UHU), then
673 submerged in liquid ACM containing 0.1% PPM. Samples were first imaged in liquid ACM
674 (plus 0.1% PPM), then submersion medium was changed to ACM plus desired concentration
675 of NaCl (plus 0.1% PPM) by first rinsing with 3~5 mL target solution, then soaked in target
676 solution for 5 minutes before imaging. Because of the reduced signal in hyperosmotic
677 solutions, possibly due to the altered refractive index, stronger gain was used to reach
678 comparable signal intensity. Osmolality was converted to osmotic pressure following $\Pi =$
679 $MiRT$ based on measurements using a cryoscopic osmometer (Osmomat 030, Gonotec).

680

681 **Finite element method (FEM) indentation simulation**

682 Inflation and indentation simulations were performed in MorphoMechanX
683 (<http://www.mpipz.mpg.de/MorphoGraphX/MorphoMechanX/>), with a procedure analogous to
684 the one explained in Mosca et al., 2017 [46] and the possibility to specify individual pressures
685 in each cell as new feature (shared walls will have a net pressure assigned given by the
686 difference of the pressure contribution between the two wall sides). For each meristem, a
687 surface projection of the L1 anticlinal walls obtained from confocal microscopy was
688 segmented and extruded to the average anticlinal wall height as observed in the template (5
689 μm for untreated and 10 μm for oryzalin-treated) with MorphoGraphX [78]. This generates a
690 multicellular template made of triangular membrane elements, shared vertexes and faces
691 between two cells are merged. The extruded meshes keep the average overall organ curvature.
692 In order to give the extruded cells a more realistic rest curvature (in the unpressurized state),
693 both meshes were pre-inflated with a small pressure (0.05 MPa for untreated and 0.15 MPa
694 oryzalin-treated SAM) and saved as the rest configuration. Indeed, AFM scan images (Figure
695 S5F) showed that plasmolysed cells are relatively flat. Both meshes were refined around the
696 indentation points to increase the accuracy of the indentation simulations. The untreated mesh
697 used in the indentation simulation and curvature analysis has an average edge size of 0.1 μm
698 near the indentation points and increases to 0.5 μm far away from those points. The oryzalin-
699 treated mesh has instead an average edge size of 0.2 μm and 1 μm near and far from the

700 indentation the indentation areas, respectively.

701 The cell wall was modelled as a Saint-Venant Kirchhoff material represented by membrane
702 elements with zero transversal stress and mathematically prescribed thickness [46]. The two
703 templates were assigned the following material properties:

704 - isotropic material, 200 MPa Young's modulus, 0.3 Poisson ratio;

705 - cell wall thickness of 0.19 μm and 0.74 μm for the untreated and oryzalin-treated
706 meristem, following experimental data.

707 A turgor pressure of 2MPa was assigned to each cell in both templates for the null
708 hypothesis case. A variable pressure around the chosen average of 2 MPa was assigned in a
709 second round of simulations on the individual cells for untreated and oryzalin-treated
710 meristems: the cell pressure variations were scaled so to reproduce the variation inferred
711 experimentally.

712 After the pressure values were assigned the templates are inflated until the force equilibrium
713 is reached, i.e. until residual forces are small enough (mean of average force norm and
714 maximal force norm). After the pressure values were assigned the templates are inflated until
715 the force equilibrium is reached (sum of the forces squared). With the chosen parameters, the
716 average cell height after inflation is similar to the average height observed from the confocal
717 stacks for the reference templates (6.8 μm for untreated and 14.5 μm for oryzalin-treated) for
718 the uniform 2 MPa assigned pressure, some variability is observed in the variable pressure
719 template. Afterwards the bottom of the template (bottom anticlinal cell walls) was blocked in
720 all space degrees of freedom to simulate the presence of the supporting inner tissue during the
721 indentation process.

722 The inflated template, with bottom vertices blocked is saved and used as starting point for the
723 indentation simulations.

724 The indentation is modelled as in [46] and is performed in the global z-direction as given by
725 the confocal images. The indentation process is performed on each cell independently, where

726 the specific indentation point is chosen to be close to the uppermost anticlinal wall location in
727 each cell, so to have near-perpendicular indentation, like in experiments. As in analysis of
728 AFM experiments, the stiffness of the untreated cell was computed as the slope of the
729 indentation curve at 0.5 μm indentation depth, with the reaction forces on the indenter
730 between 0.3 and 0.7 μm depth used for slope computation. For the oryzalin-treated, given the
731 thicker walls, the indentations were deeper and the stiffness was computed around 1 μm
732 indentation depth (reaction forces between 0.8 and 1.2 μm).

733 For both meshes, a refinement analysis was performed to verify the accuracy of the
734 simulation results (test performed on the uniform pressure case). The results are reported in
735 Table S2. We considered the variation of the coarse oryzalin mesh so small to justify using it
736 for the AFM and curvature comparison analysis, while we preferred using the refined mesh
737 for the untreated to reduce the error due to mesh resolution.

738

739 **Robustness of pressure deduction**

740 *Choice of parameters to deduce turgor pressure.* We determined surface topography of the
741 SAM with AFM and then performed indentations near the centre of cells to have near-
742 perpendicular indentation and minimize any bias due to surface slope. Both mean curvature
743 κ_M and Gaussian curvature κ_G of outer cell walls directly contribute to the capacity of turgor
744 pressure sustenance [38,39,43], and were directly determined from AFM scan images.

745 Outer cell wall thickness was measured from TEM and serial block-face imaging SEM
746 sections. As previously suggested in tomato [44], thickness is not very variable between cells
747 or within cells in Arabidopsis SAM, with untreated meristem $t_u = 179 \pm 7$ nm (mean \pm SEM)
748 and oryzalin $t_o = 742 \pm 29$ nm (Figure S3A-C). Based on previous work [45], we used the
749 indentation depth range 1% to 10% of maximal force (corresponding to approximately 0 to
750 150 nm) for the determination of apparent Young's modulus, E , in both untreated and oryzalin
751 samples (Figure 3B and 3E). Given the difference in cell curvature between conditions
752 (Figure S3), we determined indentation stiffness, k , using the depth range 15% to 30% of
753 maximal applied force (approximately 0.3 to 0.5 μm) for untreated and 75% to 99% of

754 maximal force (approximately 1.1 to 1.5 μm) (Figure 3C and 3E); this range was chosen so
755 that depth is greater than wall thickness (to minimize cell wall contributions to k) and the
756 deformed region of the cell remains smaller than its size (to minimize the contributions of
757 neighbouring cells to k), to be in the range of validity of the pressurized shell model as in
758 previous work [40].

759 To further validate this choice of depth ranges, we implemented realistic indentation using a
760 membrane indentation FEM model following Mosca et al., 2017 [46]. We constructed two
761 realistic templates (untreated- and treated-like) from confocal images; the surface was meshed
762 and one layer of cells was constructed to represent the epidermis, with uniform values of cell
763 wall thickness taken from our EM-based measurements and same cell dimensions as in
764 confocal images; all cells were inflated by turgor pressure (STAR Methods, Figure 5). We
765 performed indentations on the exact corresponding cells indented experimentally from these
766 two templates, excluding cells at periphery of the template to avoid boundary effects. In the
767 depth ranges corresponding to experiments, the deformation of neighbouring cells was
768 generally negligible, indicating that the depth range chosen enables cell-level measurements.

769 Note that these depth ranges for untreated SAMs differ from the larger values (1 to 2 μm)
770 used in preliminary experiments [41], which were interpreted using supracellular curvature
771 (unlike here) and were chosen to reveal supracellular pressure (averaged over cells and
772 possibly over cell layers) for comparison with the large-scale pressure obtained using
773 indentation with a large flat tip (100 μm diameter).

774 *Measurements reflect cellular turgor.* We now present the main arguments supporting that the
775 value inferred reflects cellular pressure. We first note that the deduction of pressure, P , is
776 relatively insensitive to variability in thickness (as described in [40]), and change in thickness
777 by 1 \times standard deviation (SD) only alters the coefficient of variance (CV) of P by 3% and 9%
778 for untreated and oryzalin samples respectively, both significantly smaller than the
779 intercellular P variability (untreated 21% and oryzalin 15%).

780 Modulus, E , thickness, t , curvatures, κ_M and κ_G , and indentation stiffness, k , are all used in the
781 formula [40] that yields pressure, P . With the intracellular variations of t being small and the

782 curvatures being computed at cell scale, we computed subcellular variability of E , k , and P
783 (intracellular coefficients of variation) and found that E and k show significantly higher
784 variability than P (Figure S4D and Figure S4M), which agrees with previous work [40], and
785 confirms that P deduction is less sensitive to subcellular variability in E or k . Additionally, we
786 found that E showed relatively comparable subcellular and intercellular variability (Figure
787 S4E-E' and Figure S4N-N'), as previously observed [45,79], whereas P showed significantly
788 bigger heterogeneity between cells than subcellular variability (Figure S4E'' and Figure
789 S4N''). All these indicate that P deduction is cell-specific, and that variability in cell wall
790 mechanics does not account for deduced pressure heterogeneity.

791 To assess quantitatively the values of P , we used an incipient plasmolysis assay to determine
792 the osmotic pressure of SAMs, and found that untreated meristems had a rather invariable
793 osmolarity of about 0.5 Osm (similar to values reported in tomato by Nakayama et al., 2012
794 [80]), while oryzalin samples showed a wider variability of 0.6 to 1.0 Osm (Figure S5). The
795 corresponding values of osmotic pressure, respectively of 1.2 MPa and 2.0 MPa, are
796 comparable to the values of turgor, 2.62 ± 0.03 MPa and 1.21 ± 0.11 MPa, (Figure S4A and
797 S4J) for untreated and for oryzalin treated, respectively. Note that oryzalin-treated SAMs are
798 significantly more variable than untreated for both osmotic and turgor pressure. However, the
799 average values obtained with AFM are higher than osmotic pressure for untreated and lower
800 for oryzalin.

801 In order to understand the source of this discrepancy, we used thin-shell indentation FEM
802 model with the null hypothesis that turgor pressure is uniform (2 MPa, rounded from
803 experimental values). We analysed FEM force-depth curves following the same protocol as in
804 experiments and inferred pressure accordingly. We found that our protocol overestimated
805 pressure by approximately 10~20% in untreated-like template and underestimated pressure by
806 approximately 30~40% in oryzalin, partially coinciding with the discrepancy between AFM-
807 deduced turgor pressure and osmotic pressure from incipient plasmolysis. The coefficient of
808 variation (CV), however, of deduced pressure was lower for FEM (5% for untreated-like,
809 19% for treated-like) than for AFM (22% for untreated, 28% for oryzalin-treated), indicating
810 that our protocol for deducing pressure might generate a constant relative error, but would not

811 introduce a bias according to cell size, tissue context, or other factors (also see below).

812 Alternative explanations of this discrepancy would be that solute penetration differs between
813 untreated and treated SAMs or that they react differently to osmotic treatment. Altogether, the
814 values of turgor found with AFM are in semi-quantitative agreement with the values of
815 osmotic pressure deduced from incipient plasmolysis.

816 Finally, we performed osmotic treatments on oryzalin-treated SAMs and measured turgor
817 with AFM. The measured turgor pressure is reduced, as expected (Figure S5). Note that the
818 decrease in turgor is about 2-fold smaller than expected from external osmolality, possibly
819 due to osmolyte uptake by cells, osmoregulation in response to treatment or the systematic
820 under-estimation by AFM in oryzalin-treated SAM.

821 *Turgor varies according to cell topology and cell size.* We now discuss biases that could affect
822 our conclusions about the trend of pressure versus cell topology and size. We note beforehand
823 that such trend is robust to normalisation and to definition of topology categories (Figure S4).

824 We examined whether this trend may be caused by trends in cell wall thickness or modulus,
825 E , or by trends in stiffness, k . There is no correlation between thickness and cell size (Pearson
826 correlation coefficient $R = -0.10$, $p = 0.65$, Figure S3). So, thickness only introduces small
827 unbiased noise, and it cannot account for the P heterogeneity. We found that E and k showed
828 no significant correlation to cell neighbour number N in untreated SAMs (Figure S3),
829 indicating that there is no systemic bias to P heterogeneity. In oryzalin-treated SAMs,
830 however, both E and k showed weak positive correlation to N (Figure S3), which is opposite
831 to the P vs N anticorrelation. This is interesting, because the higher P in $N = 4$ cells cannot be
832 explained by lower E and k . This indicates that, although feedback from shape on E (in
833 lowering E) may be present in oryzalin-treated meristems, P heterogeneity is not a direct
834 consequence of feedbacks from wall tension or cell geometry/topology on wall stiffness.

835 Next, we tested whether such trend could be due to the deduction of pressure based on local
836 cell shape while the packing of neighbouring cells would influence the measurement of
837 stiffness, k . We examined the variability of k in FEM simulations with homogeneous pressure
838 (as introduced above) and found that k variability differs from experiments, notably in

839 untreated SAMs (Figure 5H and 5L). Accordingly, the null hypothesis of uniform turgor is not
840 consistent with experimental data. We then used the same templates and prescribed
841 heterogeneous pressure, P , scaled around the average 2 MPa of the null hypothesis, following
842 the P measured experimentally in the corresponding cells. We found that, by implementing
843 variable P , FEM stiffness and curvature correlate much better with experiments for untreated
844 meristem (Figure 5J and 5K), while stiffness correlates much better with experiments for
845 treated meristem (Figure 5N). This indicates that pressure variation is required to recapitulate
846 SAM tissue topography and AFM indentations results, while the contribution of cell packing
847 to the measured variability is negligible with our magnitude of indentation. Nevertheless,
848 FEM simulations do not recapitulate curvature variations of treated SAM, suggesting that an
849 additional hypothesis would be needed to fully account for this case.

850 Moreover, we found that turgor pressure heterogeneity may be removed when sample is
851 osmotically challenged: the same SAM shows heterogeneous pressure when turgid and
852 homogeneous pressure when at intermediate turgidity (Figure S5). This shows that the AFM
853 approach is not technically biased by tissue topology and/or cell size.

854 Finally, as neither the classic pressure probe nor the pico gauge [47] (personal
855 communication) can be applied to cells as small as in the shoot apical meristem, we used cell
856 side wall convexity as a proxy for differences in turgor, because cells with higher pressure
857 would be expected to bulge out into cells with lower pressure (Figure S4) [50]. We
858 constructed a weighted index, wCI, to quantify cell convexity (Figure S4). We found that
859 convexity significantly anticorrelates with number of neighbours, in agreement with the
860 pressure trends. In addition, convexity better correlates with cell topology than with cell area,
861 consistent with the prediction of the hydraulic-mechanical model. Finally, convexity also
862 correlates with pressure.

863

864 **Mechanical-hydraulic modelling**

865 *Summary.* We build a vertex-based model of plant tissues at cellular level that couples
866 osmosis-driven hydraulic fluxes between cells and from apoplast with a fixed water potential,

867 and cell wall mechanics which resists and grows under tension. Turgor and growth rate
 868 heterogeneities emerge from this coupling and from the heterogeneities in cells sizes and
 869 topology (number of neighbours).

870 We consider a collection of N polygonal cells $i = 1, \dots, N$ that form a mesh; this mesh
 871 evolves with the appearance of new cells because of cell division. Given the topology, the
 872 mesh is fully characterized by the position of the vertices. The walls are given a height h and
 873 a thickness w .

874 *Cell wall rheology.* The cell walls are modelled as a visco-elasto-plastic material, which
 875 would be equivalent to the Ortega model [20] in the case of an elongating cell. Let σ_k be the
 876 stress of a wall segment k ; the constitutive law writes $\sigma_k = E_k \varepsilon_k^e$ where E_k is the elastic
 877 modulus and ε_k^e is the elastic deformation of the wall. Let l_k be the length of segment k , the
 878 rate of change of ε_k^e is given by:

$$879 \quad \frac{d\varepsilon_k^e}{dt} + \Phi_k^w E_k \max(0, \varepsilon_k^e - \varepsilon_k^Y) = \frac{1}{l_k} \frac{dl_k}{dt}$$

880 where Φ_k^w is the extensibility and ε_k^Y is the yield deformation of segment k . Equivalently, we
 881 could define a yield stress.

882 *Mechanical equilibrium.* Let P_i be the turgor pressure in each cell i . The tissue being at every
 883 moment in a quasi-static equilibrium, pressure forces on wall edges and elastic forces within
 884 walls balance exactly at each vertex v :

$$885 \quad \frac{1}{2} \sum_{k \in f(v)} \Delta_k P A_k \mathbf{n}_k + \sum_{k \in f(v)} E_k \varepsilon_k^e a_k \mathbf{e}_{k,v} = 0$$

886 Where $f(v)$ is the set of walls adjacent to junction v , and $\Delta_k P = P_{k_1} - P_{k_2}$ is the pressure
 887 jump across wall face k , with $k_1 < k_2$ as indices of the cells separated by face k , $A_k = h l_k$ is
 888 the area of the face k on which pressure is exerted, \mathbf{n}_k is the normal vector to face k , oriented
 889 from cell k_1 to cell k_2 , and $a_k = hw$ is the cross-section of the face, on which the elastic stress
 890 is exerted; finally, $\mathbf{e}_{k,v}$ is the unit vector in the direction of face k , oriented from junction v to
 891 the other end of face k . In the case of a single cylindrical cell for which growth is restricted to

892 its principal direction, the model is equivalent to the Lockhart-Ortega model.

893 *Fluxes.* For each cell i , the apoplastic pathway is represented as a flux U_i^a (in volume per
894 time unit) from the apoplast of constant water potential Ψ^a through a perfectly semi-
895 permeable membrane: $U_i^a = A_i L_i^a (\Delta\Pi - P_i)$, where A_i is the area of each cell in contact with
896 the apoplast, L_i^a is the corresponding water conductivity, $\Delta\Pi = \pi_i + \Psi^a$ is assumed constant,
897 and π_i is the osmotic pressure of cell i .

898 The symplasmic pathway corresponds to flows that occur through plasmodesmata, channels
899 between cells that convey both water and solutes. The symplasmic flows thus only depend on
900 turgor pressure difference. Let L_{ij} be the symplasmic water conductivity corresponding to the
901 interface between two neighbour cells i and j , and A_{ij} their contact area, both assumed
902 symmetric: $L_{ij} = L_{ji}$ and $A_{ij} = A_{ji}$. The symplasmic flux U_{ji}^s (in volume per time unit) from
903 cell j to i is defined by:

$$904 \quad U_{ji}^s = A_{ij} L_{ij}^s (P_j - P_i)$$

905 Finally, the total water flux for cell i is the sum of the apoplastic flux U_i^a and the symplasmic
906 fluxes U_{ji}^s with all its neighbors, so that its volume variation can be expressed as:

$$907 \quad \frac{dV_i}{dt} = A_i L_i^a (\Delta\Pi - P_i) + \sum_{j \in n(i)} A_{ij} L_{ij}^s (P_j - P_i)$$

908 where $n(i)$ is the set of neighbours of cell i .

909 *Cell division.* We implemented the Willis-Refahi rule [35], in which the division volume is
910 given by $V_0 = f V_b + \mu_b (2 - f + Z)$, where $f = 0.5$, V_b is the volume at birth, $\mu_b = 3.31$ is
911 the mean birth volume and Z is a Gaussian noise with zero mean and $(4\sigma_d^2 - f^2\sigma_b^2)^{1/2}$
912 standard deviation, with $\sigma_b = 0.2$ and $\sigma_d = 0.1$.

913 *Numerical resolution.* In the Lockhart-Ortega model, the compatibility between wall
914 elongation and cell volume increase is automatically enforced through the geometrical
915 constraint of unidirectional growth that leads to equal relative growth rate of the cell and

916 strain rate of the walls. In our multicellular model, this equality is no longer true. Instead, the
917 lengths $l(X)$ of the edges and the volumes $V(X)$ of the cells are expressed as functions of the
918 positions X of the vertices; then, given an initial position X of the vertices and elastic
919 deformation ε^e of the edges, the equations of wall rheology, mechanical equilibrium, and
920 water fluxes form a closed set of equations with respect to the unknowns X , P , and ε^e that
921 allow to predict their evolution.

922 To give an idea of the mathematical complexity of the problem, one may consider the
923 following example: in a connected tissue, if one cell is stretched and forced to increase its
924 volume, an equal volume of water has to enter the cell, either from the apoplastic
925 compartment or the neighbour cells. In the latter case, pressure should drop in the neighbour
926 cells, which should attract water from their own neighbours, and this could propagate to
927 further cells depending on the geometry of the tissue and the effective parameters. Volume
928 and therefore positions of the vertices could be also affected. Finally, one can see that the
929 coupling between hydraulics and mechanics implies long range interactions where pressure
930 plays a key role.

931 We developed an original algorithm and implemented it in an in-house code, where at each
932 time step, the mechanical equilibrium is resolved under constraints on the cell volume (from
933 the water fluxes), and constraints on the cell edges (from the rheological law of the walls).
934 This was implemented in Python and Julia languages, using the open source python libraries
935 NumPy, SciPy, and the Topomesh class from the OpenAlea project
936 ([http://openalea.gforge.inria.fr/doc/vplants/container/doc/html/container/openalea_container_t](http://openalea.gforge.inria.fr/doc/vplants/container/doc/html/container/openalea_container_topomesh_ref.html)
937 [opomesh_ref.html](http://openalea.gforge.inria.fr/doc/vplants/container/doc/html/container/openalea_container_topomesh_ref.html)), and the open source Julia library NLSolve
938 (<https://github.com/JuliaNLSolvers/NLsolve.jl>). This algorithm is described in more detail in
939 a separate publication [30].

940 The computations were run on a Dell precision Tower 7810 computer with a 3.6GHz Intel
941 Xeon E5 processor, 64 GB of RAM, and running Linux Debian Stretch. The typical
942 computing time was a few days for each computation.

943 *Parameterization of the model.* The reference values of the parameters were chosen based on

944 the literature or on our experiments (Table S1), except for α^s , for which no data is available
 945 and was conservatively ascribed an intermediate value of 0.5. Model behaviour was explored
 946 by changing non-dimensional parameter values as explained in the last section of the
 947 modelling method.

948 *Procedure for the computations.* We first run in parallel three computations with cell division
 949 to around 300 cells. To mimic untreated case, simulations continue until around 600 cells. To
 950 mimic the oryzalin treatment, the current states of the “untreated” computations at around 300
 951 cells are used as initial conditions for the oryzalin case: division is stopped, and we run
 952 computations either with the same effective parameters, or with some parameters modified so
 953 that the behaviour of the oryzalin treated meristems is recovered (Table S1 and Table S3); the
 954 computations are run until the total volume has been multiplied by three from this initial state.
 955 Typical runtime for one parameter set is a few days.

956 *Vertex model exploration.* Analytical exploration in a two-cell system [30] had showed that
 957 system dynamics is mostly controlled by three dimensionless parameters. The first, α^s ,
 958 compares intercellular water conductivity to total (intercellular and transmembrane)
 959 conductivity,

$$960 \quad \alpha^s = \frac{A^s L^s}{A^s L^s + A^a L^a}$$

961 with A^a the average surface of a cell, A^s the average surface of a cell in contact with
 962 neighbouring cells, and conductivities L^a of the plasma membrane and L^s due to
 963 plasmodesmata, as introduced in the main text. The second, α^a , compares the limitation of
 964 growth by transmembrane conductivity to the combined limitation of growth by cell wall
 965 extensibility and transmembrane conductivity,

$$966 \quad \alpha^a = \frac{A^a L^a / V}{A^a L^a / V + \Phi^w h / (2w)}$$

967 where h , w , and V are average values of cell height, cell wall thickness, and cell volume,
 968 respectively. α^a can be derived rigorously for a cell growing in height with constant radius,
 969 and hence a constant A^a/V ratio. Here, we use it to qualitatively describe the fact that a cell

970 with constant height and increasing radius has a decreasing A^a/V ratio, and therefore that the
 971 transmembrane conductivity becomes more limiting. Both α^s and α^a are bound between 0
 972 and 1. The third parameter, θ , assesses the osmotic drive of growth by comparing the cross-
 973 membrane osmotic pressure difference, $\Delta\Pi$, and a representative threshold pressure for
 974 growth to occur, P^Y ,

$$975 \quad \theta = \Delta\Pi / P^Y$$

976 Contrary to the Lockhart-Ortega model that was formulated at cell scale, our model accounts
 977 for specific cell wall geometry and mechanical properties. Accordingly, we express the yield
 978 pressure in terms of the yield strain ε^Y , cell geometry and topology. We found empirically
 979 [30] that half the threshold pressure of a single hexagonal cell provides a good order of
 980 magnitude for the threshold pressure in the multicellular model and hence use

$$981 \quad P^Y = \frac{w}{2R \cos(\pi/N)} E \varepsilon^Y$$

982 where R is a representative cell size (related to V/A^a), E is cell wall elastic modulus and the
 983 number of cell neighbours is $N = 6$ (Figure S1C and S1D) [30]. The tissue globally grows if
 984 $\theta > 1$. Our first results, obtained with $\alpha^s = 1/2$, $\alpha^a = 1/2$, and $\theta = 7/3$, correspond to
 985 balanced mechanical and hydraulic limitations to growth (Figure 1I-M). We explored the
 986 parameter space by considering 4 values of θ up to $40/3$ (Figure 2 and Figure S2). As will be
 987 clarified in the last subsection, we considered $\theta = 20/3$ as a reference value (Figure 2A-E).
 988 We then decreased and increased α^s to 0.1 (low cell-to-cell conductivity) and 0.9 (high cell-
 989 to-cell conductivity), or α^a to 0.1 (growth mainly limited by transmembrane water
 990 movement) and 0.9 (growth mainly limited by cell wall), respectively (Figure 2K and Figure
 991 S2). Note that α^a values at 0.5 and 0.9 span available measurements of extensibility and
 992 conductivity [36,37] (Table S1). Next, we arrested cell divisions to test their effect (Figure
 993 2F-J). In all cases, we recovered the turgor to size/neighbour-number anticorrelation (Figure
 994 2K and Figure S2), demonstrating that pressure heterogeneity is a robust behaviour of the
 995 model.

996

997

998 **QUANTIFICATION AND STATISTICAL ANALYSIS**

999 **Force curve analysis**

1000 Turgor pressure was determined as previously reported [40], using the NanoScope Analysis
1001 software (version 1.5, Bruker). Based on previous work [45], we used the range 1 to 10%
1002 maximal indentation force (corresponding to indentation depth range 0 to 150 nm) to
1003 determine apparent Young's modulus of cell wall, E , using a Hertzian fit to the force-depth
1004 curve (Figure 3B and 3E). We determined indentation stiffness, k , using a linear fit to 15% to
1005 30% of maximal applied force (approximately corresponding to the depth range 0.3 to 0.5
1006 μm) for untreated and 75% to 99% of maximal force (approximately 1.1 to 1.5 μm) for
1007 oryzalin-treated meristems (Figure 3); these ranges were chosen so that depth is greater than
1008 wall thickness (to minimize cell wall contributions to k) and the deformed region remains
1009 smaller than cell size (to minimize the contributions of neighbouring cells to k , Figure 3C and
1010 3E), so as to be in the validity range of the pressurized shell model [40]. Note that these
1011 values of depth for untreated SAMs differ from the larger values (1 to 2 μm) used in
1012 preliminary experiments [41], which were interpreted using supracellular curvature (unlike
1013 here) and were chosen to reveal supracellular pressure (averaged over many cells and possibly
1014 over cell layers) for comparison with the large-scale pressure obtained using indentation with
1015 a large flat tip (100 μm diameter). Quality of force curves were checked empirically and by
1016 the fit coefficient of determination $r^2 > 0.99$. Cells with only low quality force curves were
1017 not analysed. Cell surface curvatures (mean and Gaussian) were estimated from AFM
1018 topographic images, with the curvature radii fitted to the long and short axes of each cell.
1019 Turgor pressure was further deduced from each force curve (100 iterations) with the electron-
1020 microscopy-determined cell wall thickness 180 nm for untreated and 740 nm for oryzalin-
1021 treated SAMs, and cell-specific turgor pressure is retrieved by averaging all turgor deductions
1022 per cell.

1023 For cell registration, confocal stacks of each meristem were obtained prior to AFM
1024 measurements by an LSM 700 confocal (Carl Zeiss). Surface projection of *GFP-LTI6b* signal

1025 was generated by the software MerryProj [81], then rescaled and rotated (affine
1026 transformation) to overlay the AFM image tiles. The resulting surface projection image was
1027 used to generate cell contour image of the whole meristemic surface using morphological
1028 segmentation plugin [82] for the software ImageJ (<https://fiji.sc/>) [83,84], while the relative
1029 positions of each AFM indentation location is then registered onto the cell contour image,
1030 along with cellular geometrical and topological analyses, using the NanoIndentation plugin
1031 (version alpha) for ImageJ [85].

1032 Since each meristem had different turgor pressure range, cellular turgor pressure was
1033 normalized to the average of each meristem for comparing cell-to-cell turgor pressure
1034 heterogeneity without meristem-specific effects.

1035

1036 **Image processing and geometric analysis**

1037 3D shell mesh and surface projection of untreated meristems were generated from confocal
1038 stacks using the level set method (LSM) addon [86] for the software MorphoGraphX (MGX
1039 version 1.0) [78]. For oryzalin-treated meristems, 2D surface projections were generated by
1040 MerryProj [81] and imported into MGX for further processing. Projected images were
1041 segmented using watershed method after manual seeding, and cell lineage between time
1042 points was manually assigned in the meristem proper. To limit Z distortion and biases due to
1043 change in inclination of the surface, which may affect analysis accuracy, only cells within 20°
1044 of inclination angle from the highest position of the SAM were included. A custom-made
1045 Python script was used to trace cell lineage between multiple time points and determine cell
1046 topology based on the anticlinal wall number exported from MGX. Areal relative exponential
1047 growth rate per hour was calculated as:

$$1048 \quad G = \frac{\ln(A_t/A_0)}{\Delta t}$$

1049 where Δt is time interval in hours, A_0 is original cellular area at time t_0 , and A_t is final area at
1050 time $t_0 + \Delta t$. Cells undergone topological changes (i.e. divided cells and cells adjacent to new

1051 division planes) during the acquisition were not included in the growth analyses. To analyse
1052 variation, cell-specific growth rate was further co-aligning by the median per SAM then
1053 stretching the distribution to the average first and third quartile positions to each data point.

1054 To enhance the confocal images in hyperosmotic solution, anisotropic diffusion filter [87] was
1055 re-implemented and applied to the raw images with the following parameters (specifications
1056 see <http://cbp-domu-forge.ens-lyon.fr/redmine/projects/anifilters/wiki>): $K = 0.3$, $\sigma = 5$, $\gamma = 0.9$,
1057 $D = 10$, 50 iterations.

1058 For figure panels, brightness and contrast of confocal images were linearly enhanced for
1059 better visual. To synchronize panel shape and size, black background with no relevant
1060 information was cropped from or added to the edge of the panels.

1061 **Statistical analysis**

1062 Data were processed using Excel 2000 (Microsoft). All Tukey box plots depict the first,
1063 second (median) and third quartiles of data distribution, with whiskers marking the
1064 lowest/highest data within 1.5 interquartile ranges (IQR) of the lower/upper quartiles. Tukey's
1065 outliers are depicted as small circles outside the whiskers. Measured parameters are reported
1066 as average plus or minus standard error of the mean (SEM). Values like turgor pressure, cell
1067 area and growth rate were also normalized to the average per meristem. After normalization,
1068 every cell was considered as one biological sample, and all linear regressions and Pearson
1069 correlations were performed on whole datasets. For simulations, cells on the edge of the mesh
1070 were not analysed due to border effect. Extremely rare polygon classes (i.e. triangle and
1071 nonagon) were not shown on the box plots in the main figures but were included in linear
1072 regression and Pearson correlation tests and were plotted in Figure S5. Kolmogorov–Smirnov
1073 test was used to distinguish cell neighbour number distribution (significance level $\alpha = 0.05$).
1074 All statistics are indicated either in text or in figure captions.

1075

1076 **DATA AND CODE AVAILABILITY**

1077 The published article includes all datasets generated or analysed during this study.

1078

1079 **SUPPLEMENTAL INFORMATION**

1080 Document S1. Figure S1-S7 and Table S1-S3

1081 **Data S1. Data from mechanical-hydraulic models. Related to Figure 1, 2, 7.**

1082 **Data S2. Data from experimental measurements. Related to Figure 3, 4, 6.**

1083 **Data S3. Simulation data from FEM indentations. Related to Figure 5.**

1084 All data presented as Excel tables. Column annotations are explained in pop-ups, which can
1085 be visualized in Microsoft Office Excel.

1086 **References**

- 1087 1. Hong, L., Dumond, M., Zhu, M., Tsugawa, S., Li, C.-B., Boudaoud, A., Hamant, O., and Roeder,
1088 A.H.K. (2018). Heterogeneity and Robustness in Plant Morphogenesis: From Cells to Organs.
1089 *Annu. Rev. Plant Biol.* *69*, 469–495.
- 1090 2. Kamimoto, K., Kaneko, K., Kok, C.Y.-Y., Okada, H., Miyajima, A., and Itoh, T. (2016).
1091 Heterogeneity and stochastic growth regulation of biliary epithelial cells dictate dynamic
1092 epithelial tissue remodeling. *eLife* *5*. Available at:
1093 <https://www.ncbi.nlm.nih.gov/pmc/articles/PMC4951195/>.
- 1094 3. Ietswaart, R., Rosa, S., Wu, Z., Dean, C., and Howard, M. (2017). Cell-Size-Dependent
1095 Transcription of FLC and Its Antisense Long Non-coding RNA COOLAIR Explain Cell-to-Cell
1096 Expression Variation. *Cell Syst.* *4*, 622-635.e9.
- 1097 4. Long, Y., Stahl, Y., Weidtkamp-Peters, S., Postma, M., Zhou, W., Goedhart, J., Sánchez-Pérez,
1098 M.-I., Gadella, T.W.J., Simon, R., Scheres, B., *et al.* (2017). In vivo FRET-FLIM reveals cell-type-
1099 specific protein interactions in Arabidopsis roots. *Nature* *548*, 97–102.
- 1100 5. Chubb, J.R. (2017). Symmetry breaking in development and stochastic gene expression.
1101 *Wiley Interdiscip. Rev. Dev. Biol.* *6*, e284.
- 1102 6. Donati, G., and Watt, F.M. (2015). Stem Cell Heterogeneity and Plasticity in Epithelia. *Cell*
1103 *Stem Cell* *16*, 465–476.
- 1104 7. Gerdes, M.J., Sood, A., Sevinsky, C., Pris, A.D., Zavodszky, M.I., and Ginty, F. (2014). Emerging
1105 Understanding of Multiscale Tumor Heterogeneity. *Front. Oncol.* *4*. Available at:
1106 <https://www.frontiersin.org/articles/10.3389/fonc.2014.00366/full> [Accessed May 17, 2018].
- 1107 8. Eldar, A., and Elowitz, M.B. (2010). Functional roles for noise in genetic circuits. *Nature* *467*,
1108 167–173.
- 1109 9. Watanabe, K., Umeda, T., Niwa, K., Naguro, I., and Ichijo, H. (2018). A PP6-ASK3 Module
1110 Coordinates the Bidirectional Cell Volume Regulation under Osmotic Stress. *Cell Rep.* *22*,
1111 2809–2817.
- 1112 10. Xie, K., Yang, Y., and Jiang, H. (2018). Controlling Cellular Volume via Mechanical and Physical
1113 Properties of Substrate. *Biophys. J.* *114*, 675–687.
- 1114 11. Guo, M., Pegoraro, A.F., Mao, A., Zhou, E.H., Arany, P.R., Han, Y., Burnette, D.T., Jensen, M.H.,
1115 Kasza, K.E., Moore, J.R., *et al.* (2017). Cell volume change through water efflux impacts cell
1116 stiffness and stem cell fate. *Proc. Natl. Acad. Sci.* *114*, E8618–E8627.
- 1117 12. Dumais, J., and Forterre, Y. (2012). “Vegetable Dynamicks”: The Role of Water in Plant
1118 Movements. *Annu. Rev. Fluid Mech.* *44*, 453–478.
- 1119 13. Stewart, M.P., Helenius, J., Toyoda, Y., Ramanathan, S.P., Muller, D.J., and Hyman, A.A. (2011).

- 1120 Hydrostatic pressure and the actomyosin cortex drive mitotic cell rounding. *Nature* 469, 226–
1121 230.
- 1122 14. Montel, F., Delarue, M., Elgeti, J., Malaquin, L., Basan, M., Risler, T., Cabane, B., Vignjevic, D.,
1123 Prost, J., Cappello, G., *et al.* (2011). Stress clamp experiments on multicellular tumor
1124 spheroids. *Phys. Rev. Lett.* 107, 188102.
- 1125 15. Rojas, E.R., and Huang, K.C. (2017). Regulation of microbial growth by turgor pressure. *Curr.*
1126 *Opin. Microbiol.* 42, 62–70.
- 1127 16. Zerzour, R., Kroeger, J., and Geitmann, A. (2009). Polar growth in pollen tubes is associated
1128 with spatially confined dynamic changes in cell mechanical properties. *Dev. Biol.* 334, 437–
1129 446.
- 1130 17. Lopez, R., Badel, E., Peraudeau, S., Leblanc-Fournier, N., Beaujard, F., Julien, J.-L., Cochard, H.,
1131 and Mouliat, B. (2014). Tree shoot bending generates hydraulic pressure pulses: a new long-
1132 distance signal? *J. Exp. Bot.* 65, 1997–2008.
- 1133 18. Beauzamy, L., Nakayama, N., and Boudaoud, A. (2014). Flowers under pressure: ins and outs
1134 of turgor regulation in development. *Ann. Bot.*, mcu187.
- 1135 19. Feng, W., Lindner, H., Robbins, N.E., and Dinneny, J.R. (2016). Growing Out of Stress: The Role
1136 of Cell- and Organ-Scale Growth Control in Plant Water-Stress Responses. *Plant Cell* 28,
1137 1769–1782.
- 1138 20. Ortega, J.K. (1985). Augmented growth equation for cell wall expansion. *Plant Physiol.* 79,
1139 318–320.
- 1140 21. Kroeger, J.H., Zerzour, R., and Geitmann, A. (2011). Regulator or driving force? The role of
1141 turgor pressure in oscillatory plant cell growth. *PLoS One* 6, e18549.
- 1142 22. Sager, R.E., and Lee, J.-Y. (2018). Plasmodesmata at a glance. *J. Cell Sci.* 131, jcs209346.
- 1143 23. Willmer, C.M., and Sexton, R. (1979). Stomata and plasmodesmata. *Protoplasma* 100, 113–
1144 124.
- 1145 24. Wille, A.C., and Lucas, W.J. (1984). Ultrastructural and histochemical studies on guard cells.
1146 *Planta* 160, 129–142.
- 1147 25. Ruan, Y.L., Llewellyn, D.J., and Furbank, R.T. (2001). The control of single-celled cotton fiber
1148 elongation by developmentally reversible gating of plasmodesmata and coordinated
1149 expression of sucrose and K⁺ transporters and expansin. *Plant Cell* 13, 47–60.
- 1150 26. Rygol, J., Pritchard, J., Zhu, J.J., Tomos, A.D., and Zimmermann, U. (1993). Transpiration
1151 Induces Radial Turgor Pressure Gradients in Wheat and Maize Roots. *Plant Physiol.* 103, 493–
1152 500.
- 1153 27. Robbins, N.E., and Dinneny, J.R. (2018). Growth is required for perception of water

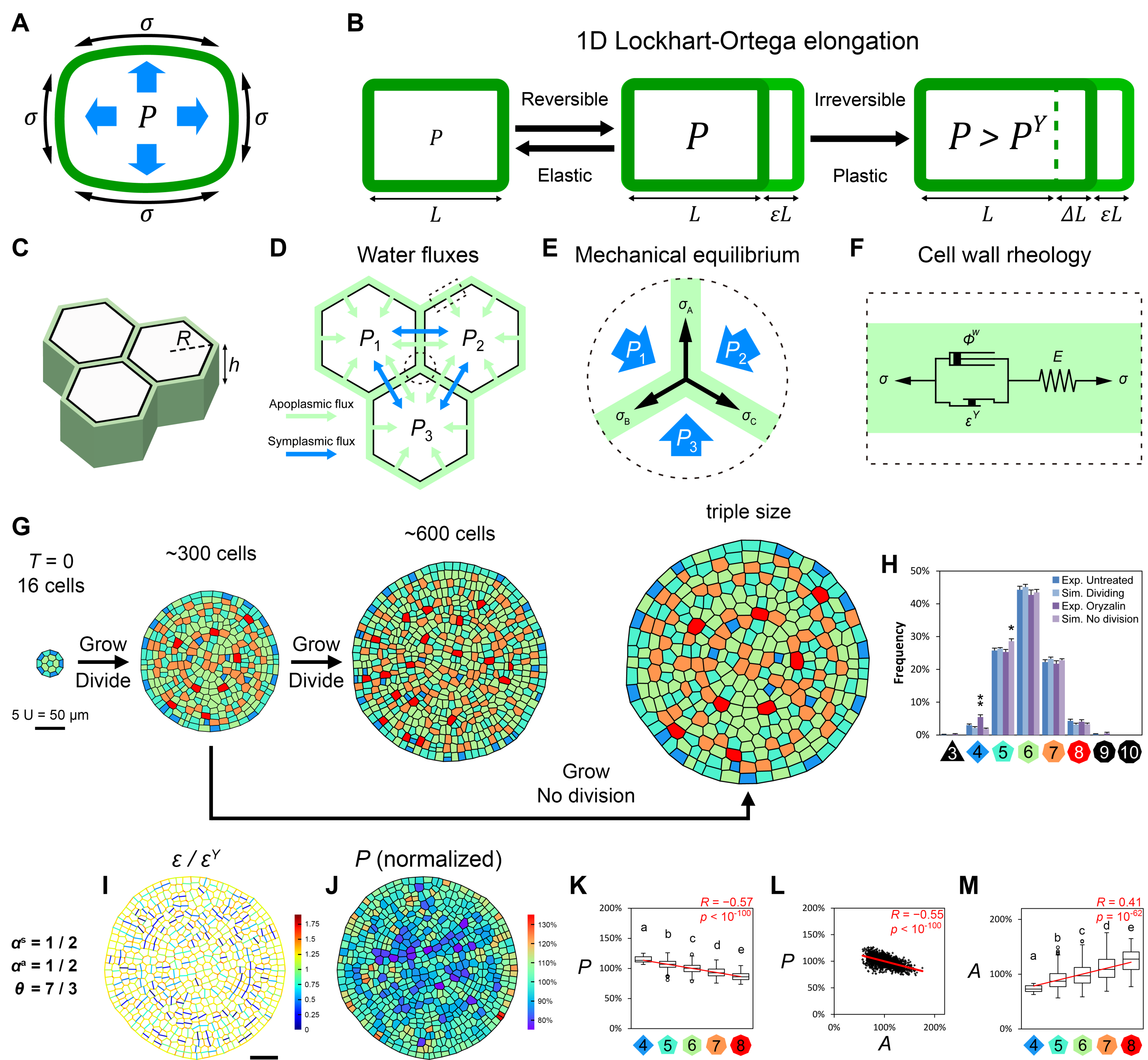
- 1154 availability to pattern root branches in plants. *Proc. Natl. Acad. Sci.* *115*, E822–E831.
- 1155 28. Corson, F., Hamant, O., Bohn, S., Traas, J., Boudaoud, A., and Couder, Y. (2009). Turning a
1156 plant tissue into a living cell froth through isotropic growth. *Proc. Natl. Acad. Sci. U. S. A.* *106*,
1157 8453–8458.
- 1158 29. Ishihara, S., Sugimura, K., Cox, S.J., Bonnet, I., Bellaïche, Y., and Graner, F. (2013).
1159 Comparative study of non-invasive force and stress inference methods in tissue. *Eur. Phys. J.*
1160 *E Soft Matter* *36*, 9859.
- 1161 30. Cheddadi, I., Génard, M., Bertin, N., and Godin, C. (2019). Coupling water fluxes with cell wall
1162 mechanics in a multicellular model of plant development. *PLOS Comput. Biol.* *15*, e1007121.
- 1163 31. Lucas, W.J., Ham, B.-K., and Kim, J.-Y. (2009). Plasmodesmata - bridging the gap between
1164 neighboring plant cells. *Trends Cell Biol.* *19*, 495–503.
- 1165 32. Kumar, N.M., and Gilula, N.B. (1996). The Gap Junction Communication Channel. *Cell* *84*,
1166 381–388.
- 1167 33. McLean, P.F., and Cooley, L. (2013). Protein Equilibration through Somatic Ring Canals in
1168 *Drosophila*. *Science* *340*. Available at:
1169 <https://www.ncbi.nlm.nih.gov/pmc/articles/PMC3819220/>.
- 1170 34. Maurel, C., Boursiac, Y., Luu, D.-T., Santoni, V., Shahzad, Z., and Verdoucq, L. (2015).
1171 Aquaporins in Plants. *Physiol. Rev.* *95*, 1321–1358.
- 1172 35. Willis, L., Refahi, Y., Wightman, R., Landrein, B., Teles, J., Huang, K.C., Meyerowitz, E.M., and
1173 Jönsson, H. (2016). Cell size and growth regulation in the *Arabidopsis thaliana* apical stem
1174 cell niche. *Proc. Natl. Acad. Sci. U. S. A.* *113*, E8238–E8246.
- 1175 36. Boyer, J.S., Cavalieri, A.J., and Schulze, E.-D. (1985). Control of the rate of cell enlargement:
1176 Excision, wall relaxation, and growth-induced water potentials. *Planta* *163*, 527–543.
- 1177 37. Cosgrove, D.J. (1985). Cell Wall Yield Properties of Growing Tissue: Evaluation by in Vivo
1178 Stress Relaxation. *Plant Physiol.* *78*, 347–356.
- 1179 38. Vella, D., Ajdari, A., Vaziri, A., and Boudaoud, A. (2012). The indentation of pressurized elastic
1180 shells: from polymeric capsules to yeast cells. *J. R. Soc. Interface* *9*, 448–455.
- 1181 39. Vella, D., Ajdari, A., Vaziri, A., and Boudaoud, A. (2012). Indentation of Ellipsoidal and
1182 Cylindrical Elastic Shells. *Phys. Rev. Lett.* *109*, 144302.
- 1183 40. Beauzamy, L., Derr, J., and Boudaoud, A. (2015). Quantifying Hydrostatic Pressure in Plant
1184 Cells by Using Indentation with an Atomic Force Microscope. *Biophys. J.* *108*, 2448–2456.
- 1185 41. Beauzamy, L., Louveaux, M., Hamant, O., and Boudaoud, A. (2015). Mechanically, the Shoot
1186 Apical Meristem of *Arabidopsis* Behaves like a Shell Inflated by a Pressure of About 1 MPa.
1187 *Front. Plant Sci.* *6*. Available at: <http://www.ncbi.nlm.nih.gov/pmc/articles/PMC4659900/>

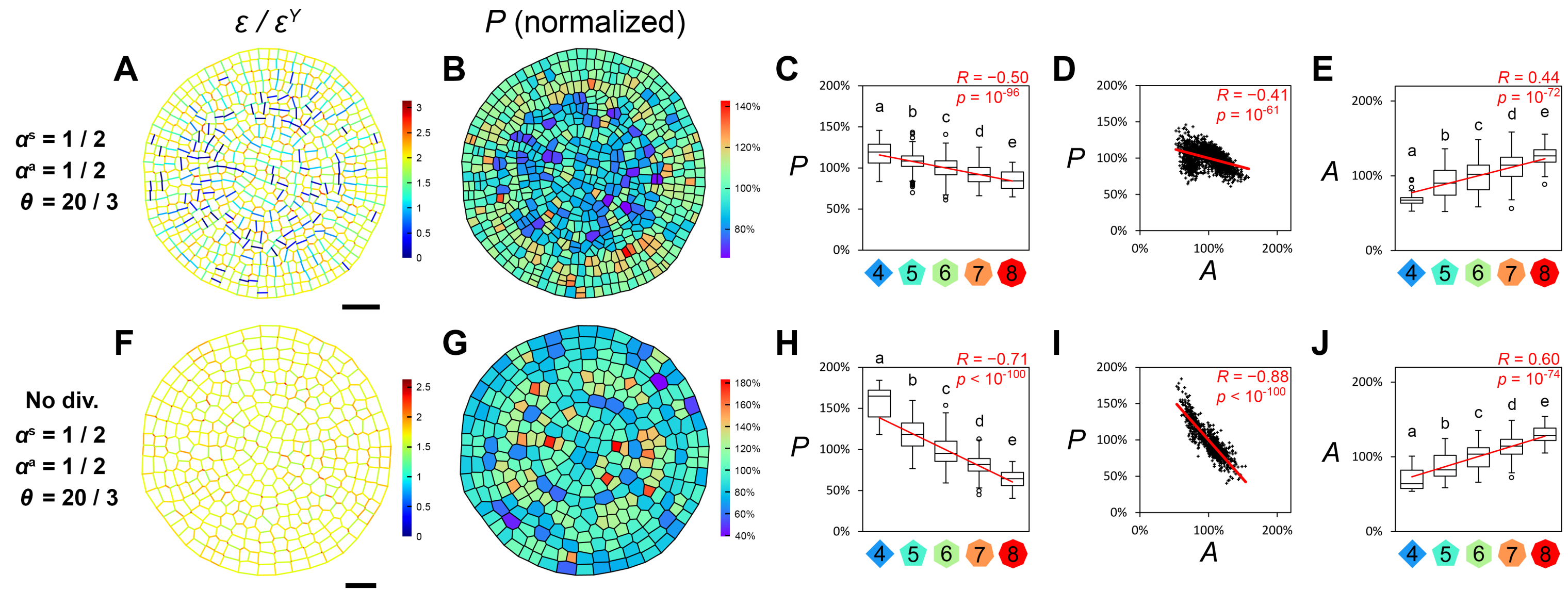
- 1188 [Accessed June 28, 2016].
- 1189 42. Malgat, R., Faure, F., and Boudaoud, A. (2016). A Mechanical Model to Interpret Cell-Scale
1190 Indentation Experiments on Plant Tissues in Terms of Cell Wall Elasticity and Turgor Pressure.
1191 *Front. Plant Sci.* 7. Available at:
1192 <https://www.frontiersin.org/articles/10.3389/fpls.2016.01351/full> [Accessed May 21, 2018].
- 1193 43. Lazarus, A., Florijn, H.C.B., and Reis, P.M. (2012). Geometry-induced rigidity in nonspherical
1194 pressurized elastic shells. *Phys. Rev. Lett.* 109, 144301.
- 1195 44. Kierzkowski, D., Nakayama, N., Routier-Kierzkowska, A.-L., Weber, A., Bayer, E., Schorderet,
1196 M., Reinhardt, D., Kuhlemeier, C., and Smith, R.S. (2012). Elastic domains regulate growth
1197 and organogenesis in the plant shoot apical meristem. *Science* 335, 1096–1099.
- 1198 45. Milani, P., Gholamirad, M., Traas, J., Arnéodo, A., Boudaoud, A., Argoul, F., and Hamant, O.
1199 (2011). In vivo analysis of local wall stiffness at the shoot apical meristem in *Arabidopsis*
1200 using atomic force microscopy. *Plant J. Cell Mol. Biol.* 67, 1116–1123.
- 1201 46. Mosca, G., Sapala, A., Strauss, S., Routier-Kierzkowska, A.-L., and Smith, R.S. (2017). On the
1202 micro-indentation of plant cells in a tissue context. *Phys. Biol.* 14, 015003.
- 1203 47. Knoblauch, J., Mullendore, D.L., Jensen, K.H., and Knoblauch, M. (2014). Pico gauges for
1204 minimally invasive intracellular hydrostatic pressure measurements. *Plant Physiol.*,
1205 pp.114.245746.
- 1206 48. Lewis, F.T. (1928). The correlation between cell division and the shapes and sizes of prismatic
1207 cells in the epidermis of cucumis. *Anat. Rec.* 38, 341–376.
- 1208 49. Gibson, W.T., Veldhuis, J.H., Rubinstein, B., Cartwright, H.N., Perrimon, N., Brodland, G.W.,
1209 Nagpal, R., and Gibson, M.C. (2011). Control of the mitotic cleavage plane by local epithelial
1210 topology. *Cell* 144, 427–438.
- 1211 50. Hamant, O., Heisler, M.G., Jönsson, H., Krupinski, P., Uyttewaal, M., Bokov, P., Corson, F.,
1212 Sahlin, P., Boudaoud, A., Meyerowitz, E.M., *et al.* (2008). Developmental Patterning by
1213 Mechanical Signals in *Arabidopsis*. *Science* 322, 1650–1655.
- 1214 51. Kwiatkowska, D. (2004). Surface growth at the reproductive shoot apex of *Arabidopsis*
1215 *thaliana* pin-formed 1 and wild type. *J. Exp. Bot.* 55, 1021–1032.
- 1216 52. Serrano-Mislata, A., Schiessl, K., and Sablowski, R. (2015). Active Control of Cell Size
1217 Generates Spatial Detail during Plant Organogenesis. *Curr. Biol.* 25, 2991–2996.
- 1218 53. Ali, O., Mirabet, V., Godin, C., and Traas, J. (2014). Physical models of plant development.
1219 *Annu. Rev. Cell Dev. Biol.* 30, 59–78.
- 1220 54. Dumond, M., and Boudaoud, A. (2018). Physical Models of Plant Morphogenesis. In
1221 *Mathematical Modelling in Plant Biology*, R. J. Morris, ed. (Cham: Springer International

- 1222 Publishing), pp. 1–14. Available at: https://doi.org/10.1007/978-3-319-99070-5_1 [Accessed
1223 October 14, 2019].
- 1224 55. Alt, S., Ganguly, P., and Salbreux, G. (2017). Vertex models: from cell mechanics to tissue
1225 morphogenesis. *Philos. Trans. R. Soc. B Biol. Sci.* 372. Available at:
1226 <https://www.ncbi.nlm.nih.gov/pmc/articles/PMC5379026/> [Accessed October 14, 2019].
- 1227 56. Weaire, D.L., and Hutzler, S. (2001). *The Physics of Foams* (Clarendon Press).
- 1228 57. Yi, H., Chen, Y., Wang, J.Z., Puri, V.M., and Anderson, C.T. (2019). The stomatal flexoskeleton:
1229 how the biomechanics of guard cell walls animate an elastic pressure vessel. *J. Exp. Bot.* 70,
1230 3561–3572.
- 1231 58. Dyson, R.J., Vizcay-Barrena, G., Band, L.R., Fernandes, A.N., French, A.P., Fozard, J.A.,
1232 Hodgman, T.C., Kenobi, K., Pridmore, T.P., Stout, M., *et al.* (2014). Mechanical modelling
1233 quantifies the functional importance of outer tissue layers during root elongation and
1234 bending. *New Phytol.* 202, 1212–1222.
- 1235 59. Forouzesh, E., Goel, A., Mackenzie, S.A., and Turner, J.A. (2013). In vivo extraction of
1236 Arabidopsis cell turgor pressure using nanoindentation in conjunction with finite element
1237 modeling. *Plant J.* 73, 509–520.
- 1238 60. Klepikova, A.V., Kasianov, A.S., Gerasimov, E.S., Logacheva, M.D., and Penin, A.A. (2016). A
1239 high resolution map of the Arabidopsis thaliana developmental transcriptome based on RNA-
1240 seq profiling. *Plant J. Cell Mol. Biol.* 88, 1058–1070.
- 1241 61. Péret, B., Li, G., Zhao, J., Band, L.R., Voß, U., Postaire, O., Luu, D.-T., Da Ines, O., Casimiro, I.,
1242 Lucas, M., *et al.* (2012). Auxin regulates aquaporin function to facilitate lateral root
1243 emergence. *Nat. Cell Biol.* 14, 991–998.
- 1244 62. Tsugawa, S., Hervieux, N., Kierzkowski, D., Routier-Kierzkowska, A.-L., Sapala, A., Hamant, O.,
1245 Smith, R.S., Roeder, A.H.K., Boudaoud, A., and Li, C.-B. (2017). Clones of cells switch from
1246 reduction to enhancement of size variability in Arabidopsis sepals. *Development* 144, 4398–
1247 4405.
- 1248 63. Sapala, A., Runions, A., Routier-Kierzkowska, A.-L., Das Gupta, M., Hong, L., Hofhuis, H.,
1249 Verger, S., Mosca, G., Li, C.-B., Hay, A., *et al.* (2018). Why plants make puzzle cells, and how
1250 their shape emerges. *eLife* 7.
- 1251 64. LeGoff, L., Rouault, H., and Lecuit, T. (2013). A global pattern of mechanical stress polarizes
1252 cell divisions and cell shape in the growing Drosophila wing disc. *Development* 140, 4051–
1253 4059.
- 1254 65. Campinho, P., Behrndt, M., Ranft, J., Risler, T., Minc, N., and Heisenberg, C.-P. (2013). Tension-
1255 oriented cell divisions limit anisotropic tissue tension in epithelial spreading during zebrafish
1256 epiboly. *Nat. Cell Biol.* 15, 1405–1414.

- 1257 66. Mao, Y., Tournier, A.L., Hoppe, A., Kester, L., Thompson, B.J., and Tapon, N. (2013).
1258 Differential proliferation rates generate patterns of mechanical tension that orient tissue
1259 growth. *EMBO J.* 32, 2790–2803.
- 1260 67. Louveaux, M., Julien, J.-D., Mirabet, V., Boudaoud, A., and Hamant, O. (2016). Cell division
1261 plane orientation based on tensile stress in *Arabidopsis thaliana*. *Proc. Natl. Acad. Sci.* 113,
1262 E4294–E4303.
- 1263 68. Gibson, W.T., and Gibson, M.C. (2009). Chapter 4 Cell Topology, Geometry, and
1264 Morphogenesis in Proliferating Epithelia. In *Current Topics in Developmental Biology* Current
1265 Topics in Developmental Biology. (Academic Press), pp. 87–114. Available at:
1266 <http://www.sciencedirect.com/science/article/pii/S0070215309890042>.
- 1267 69. Long, Y., and Boudaoud, A. (2018). Emergence of robust patterns from local rules during
1268 plant development. *Curr. Opin. Plant Biol.* 47, 127–137.
- 1269 70. Vargas-Garcia, C.A., Ghusinga, K.R., and Singh, A. (2018). Cell size control and gene
1270 expression homeostasis in single-cells. *Curr. Opin. Syst. Biol.* 8, 109–116.
- 1271 71. Ortega, J.K.E. (2019). Dimensionless Numbers to Analyze Expansive Growth Processes. *Plants*
1272 8, 17.
- 1273 72. Cutler, S.R., Ehrhardt, D.W., Griffiths, J.S., and Somerville, C.R. (2000). Random GFP::cDNA
1274 fusions enable visualization of subcellular structures in cells of *Arabidopsis* at a high
1275 frequency. *Proc. Natl. Acad. Sci.* 97, 3718–3723.
- 1276 73. Brunoud, G., Wells, D.M., Oliva, M., Larrieu, A., Mirabet, V., Burrow, A.H., Beeckman, T.,
1277 Kepinski, S., Traas, J., Bennett, M.J., *et al.* (2012). A novel sensor to map auxin response and
1278 distribution at high spatio-temporal resolution. *Nature* 482, 103–106.
- 1279 74. Benková, E., Michniewicz, M., Sauer, M., Teichmann, T., Seifertová, D., Jürgens, G., and Friml,
1280 J. (2003). Local, Efflux-Dependent Auxin Gradients as a Common Module for Plant Organ
1281 Formation. *Cell* 115, 591–602.
- 1282 75. Stanislas, T., Hamant, O., and Traas, J. (2017). Chapter 11 - In-vivo analysis of morphogenesis
1283 in plants. In *Methods in Cell Biology Cell Polarity and Morphogenesis.*, T. Lecuit, ed.
1284 (Academic Press), pp. 203–223. Available at:
1285 <http://www.sciencedirect.com/science/article/pii/S0091679X16301601>.
- 1286 76. Sassi, M., Ali, O., Boudon, F., Cloarec, G., Abad, U., Cellier, C., Chen, X., Gilles, B., Milani, P.,
1287 Friml, J., *et al.* (2014). An auxin-mediated shift toward growth isotropy promotes organ
1288 formation at the shoot meristem in *Arabidopsis*. *Curr. Biol. CB* 24, 2335–2342.
- 1289 77. Kremer, A., Lippens, S., Bartunkova, S., Asselbergh, B., Blanpain, C., Fendrych, M., Goossens,
1290 A., Holt, M., Janssens, S., Krols, M., *et al.* (2015). Developing 3D SEM in a broad biological
1291 context. *J. Microsc.* 259, 80–96.

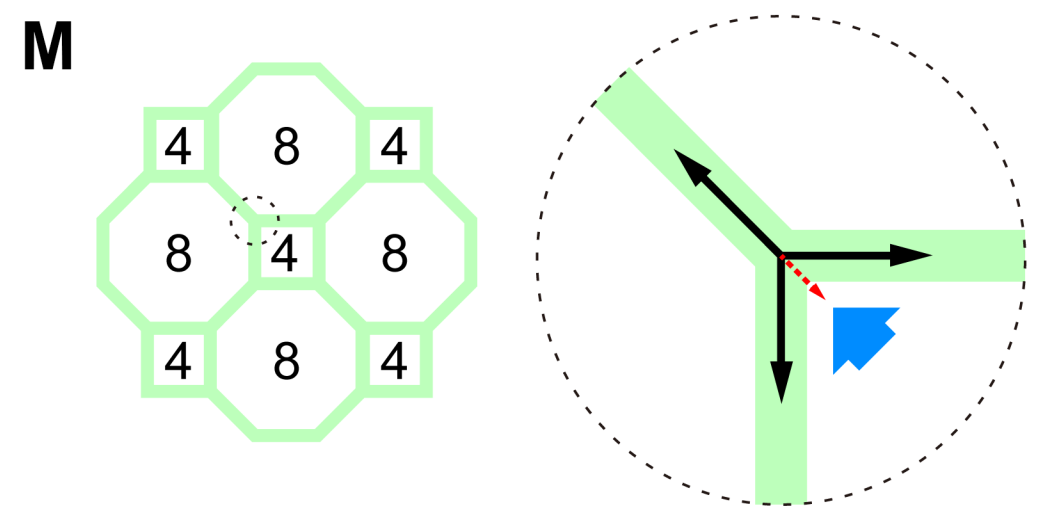
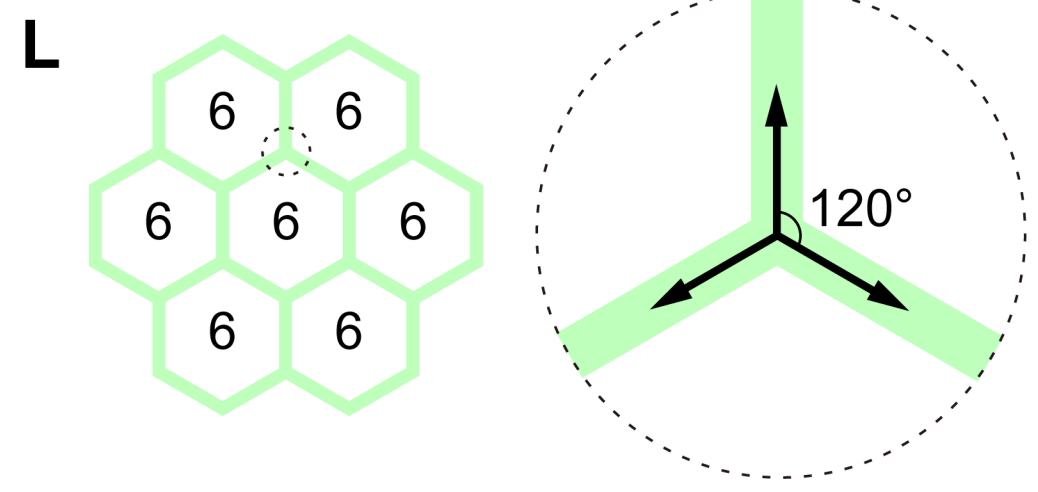
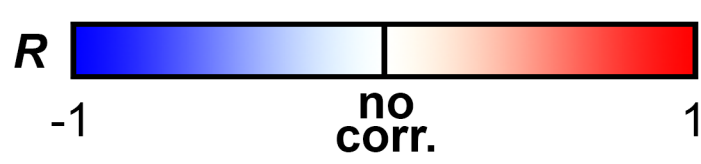
- 1292 78. Reuille, P.B. de, Routier-Kierzkowska, A.-L., Kierzkowski, D., Bassel, G.W., Schüpbach, T.,
1293 Tauriello, G., Bajpai, N., Strauss, S., Weber, A., Kiss, A., *et al.* (2015). MorphoGraphX: A
1294 platform for quantifying morphogenesis in 4D. *eLife* 4, e05864.
- 1295 79. Hong, L., Dumond, M., Tsugawa, S., Sapala, A., Routier-Kierzkowska, A.-L., Zhou, Y., Chen, C.,
1296 Kiss, A., Zhu, M., Hamant, O., *et al.* (2016). Variable Cell Growth Yields Reproducible Organ
1297 Development through Spatiotemporal Averaging. *Dev. Cell* 38, 15–32.
- 1298 80. Nakayama, N., Smith, R.S., Mandel, T., Robinson, S., Kimura, S., Boudaoud, A., and
1299 Kuhlemeier, C. (2012). Mechanical Regulation of Auxin-Mediated Growth. *Curr. Biol.* 22,
1300 1468–1476.
- 1301 81. Reuille, P.B. de, Bohn-Courseau, I., Godin, C., and Traas, J. (2005). A protocol to analyse
1302 cellular dynamics during plant development. *Plant J.* 44, 1045–1053.
- 1303 82. Legland, D., Arganda-Carreras, I., and Andrey, P. (2016). MorphoLibJ: integrated library and
1304 plugins for mathematical morphology with ImageJ. *Bioinformatics* 32, 3532–3534.
- 1305 83. Schneider, C.A., Rasband, W.S., and Eliceiri, K.W. (2012). NIH Image to ImageJ: 25 years of
1306 image analysis. *Nat. Methods* 9, 671–675.
- 1307 84. Schindelin, J., Arganda-Carreras, I., Frise, E., Kaynig, V., Longair, M., Pietzsch, T., Preibisch, S.,
1308 Rueden, C., Saalfeld, S., Schmid, B., *et al.* (2012). Fiji: an open-source platform for biological-
1309 image analysis. *Nat. Methods* 9, 676–682.
- 1310 85. Mirabet, V., Dubrulle, N., Rambaud, L., Beauzamy, L., Dumond, M., Long, Y., Milani, P., and
1311 Boudaoud, A. (in press). NanoIndentation, an ImageJ Plugin for the Quantification of Cell
1312 Mechanics. *Methods Mol. Biol.*
- 1313 86. Kiss, A., Moreau, T., Mirabet, V., Calugaru, C.I., Boudaoud, A., and Das, P. (2017).
1314 Segmentation of 3D images of plant tissues at multiple scales using the level set method.
1315 *Plant Methods* 13, 114.
- 1316 87. Schmidt, T., Pasternak, T., Liu, K., Blein, T., Aubry-Hivet, D., Dovzhenko, A., Duerr, J., Teale, W.,
1317 Ditengou, F.A., Burkhardt, H., *et al.* (2014). The iRoCS Toolbox – 3D analysis of the plant root
1318 apical meristem at cellular resolution. *Plant J.* 77, 806–814.
- 1319
- 1320

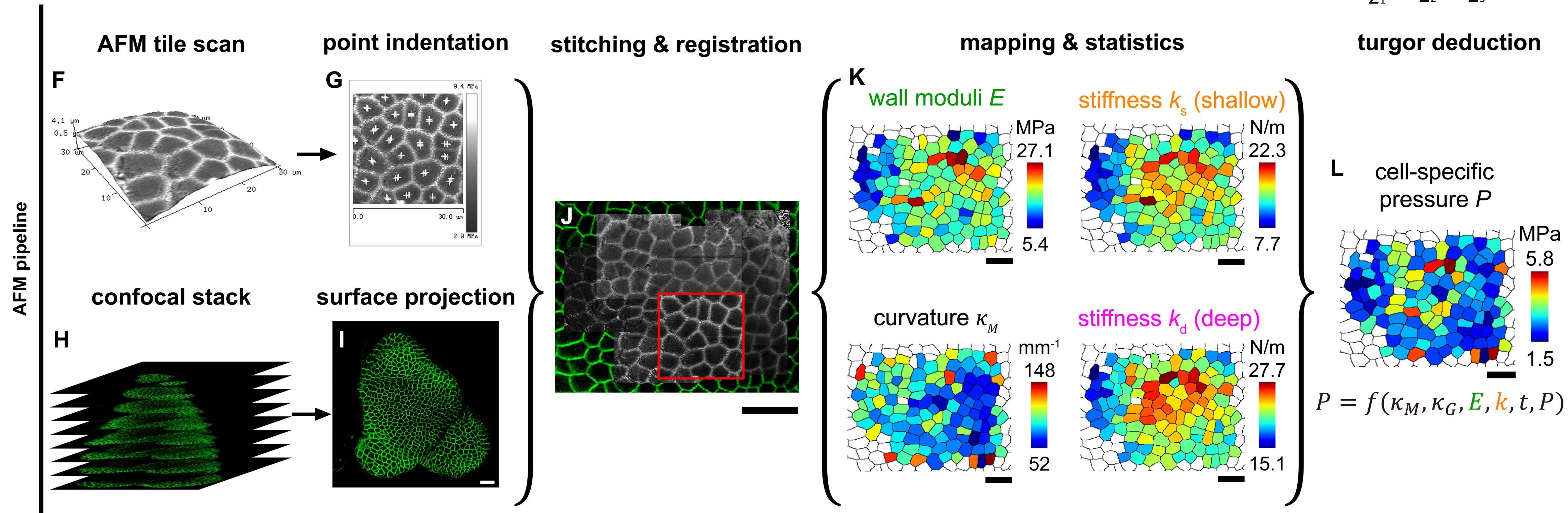
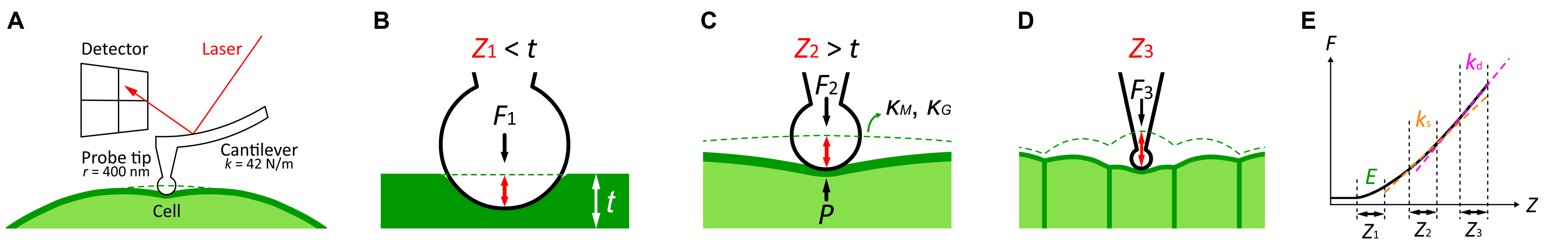




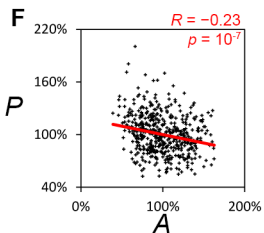
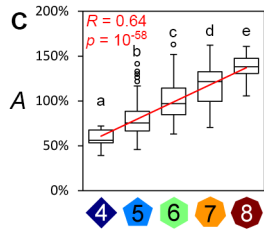
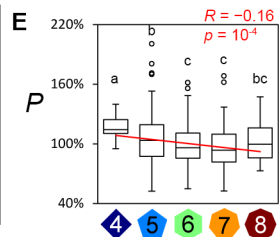
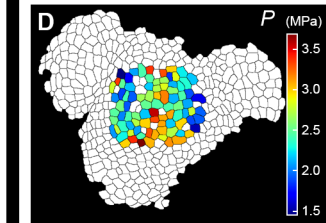
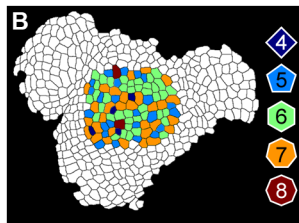
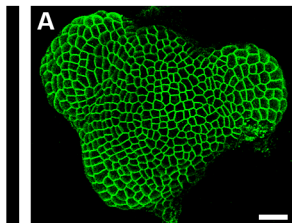
K Correlation between

Dimensionless parameters			A, N	P, N	P, A
$\alpha^s = 1/2$	$\alpha^a = 1/2$	$\theta = 7/3$	0.41	-0.57	-0.55
$\alpha^s = 1/2$	$\alpha^a = 1/2$	$\theta = 10/3$	0.49	-0.56	-0.54
$\alpha^s = 1/2$	$\alpha^a = 1/2$	$\theta = 20/3$	0.44	-0.50	-0.41
$\alpha^s = 1/10$	$\alpha^a = 1/2$	$\theta = 20/3$	0.44	-0.52	-0.38
$\alpha^s = 9/10$	$\alpha^a = 1/2$	$\theta = 20/3$	0.42	-0.42	-0.47
$\alpha^s = 1/2$	$\alpha^a = 1/10$	$\theta = 20/3$	0.48	-0.59	-0.42
$\alpha^s = 1/2$	$\alpha^a = 9/10$	$\theta = 20/3$	0.44	-0.46	-0.48
$\alpha^s = 1/2$	$\alpha^a = 1/2$	$\theta = 10$	0.47	-0.49	-0.40
$\alpha^s = 1/2$	$\alpha^a = 1/2$	$\theta = 40/3$	0.50	-0.51	-0.42

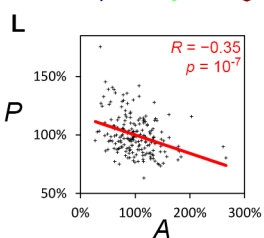
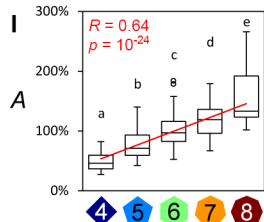
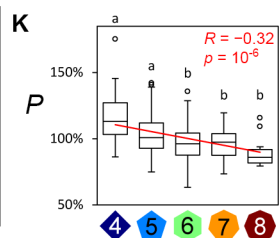
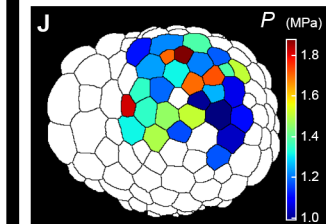
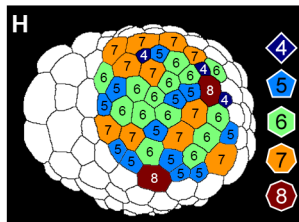
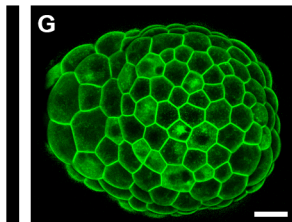


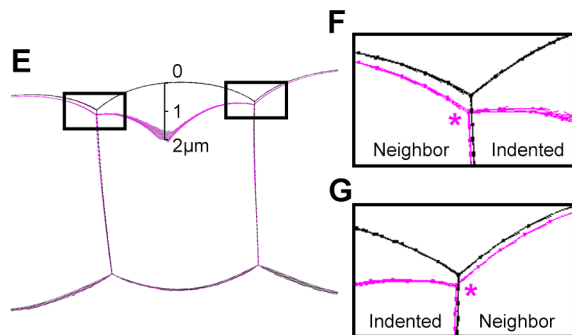
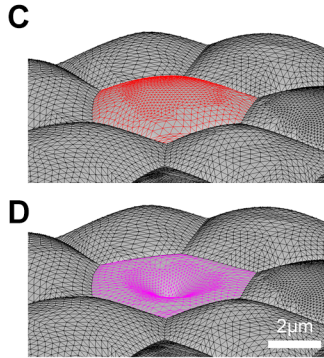
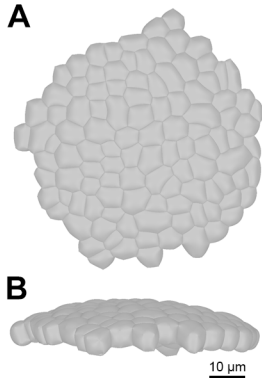


Untreated



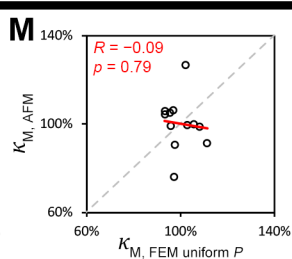
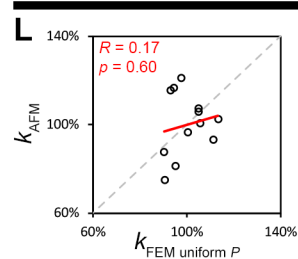
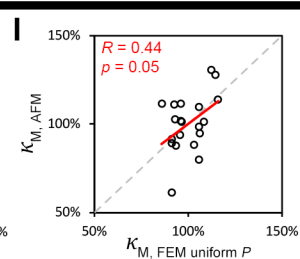
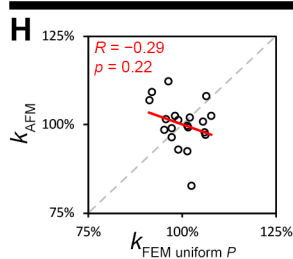
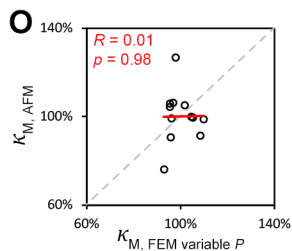
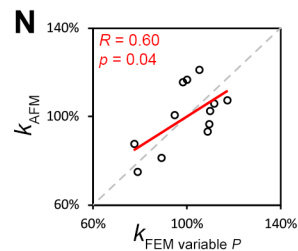
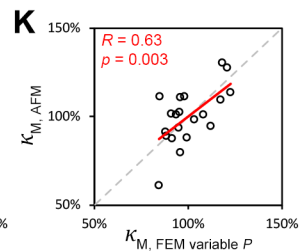
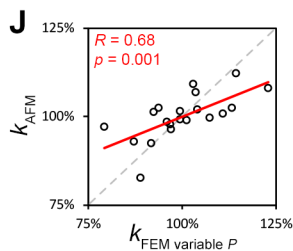
Oryzalin-treated



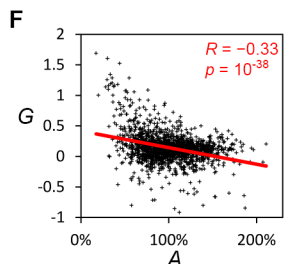
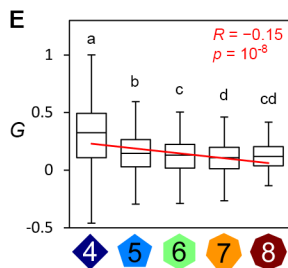
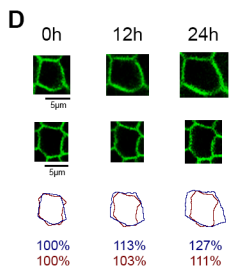
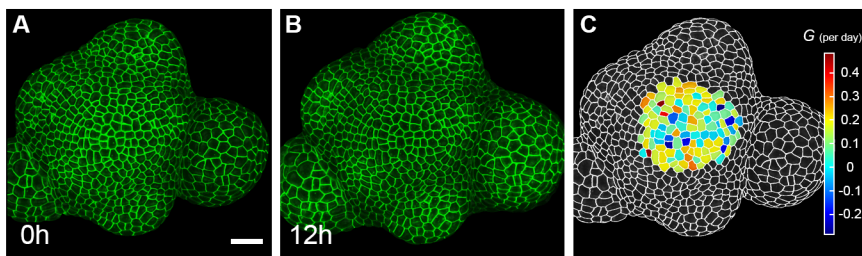


Untreated

Oryzalin-treated

uniform P variable P 

Untreated



Oryzalin-treated

